THE STRUCTURE OF THE LOCAL INTERSTELLAR MEDIUM. IV. DYNAMICS, MORPHOLOGY, PHYSICAL PROPERTIES, AND IMPLICATIONS OF CLOUD-CLOUD INTERACTIONS[1]

Seth Redfield[2,3] and Jeffrey L. Linsky[4]

ABSTRACT

We present an empirical dynamical model of the LISM based on 270 radial velocity measurements for 157 sight lines toward nearby stars. Physical parameter measurements (i.e., temperature, turbulent velocity, depletions) are available for 90 components, or one-third of the sample, enabling initial characterizations of the physical properties of LISM clouds. The model includes 15 warm clouds located within 15 pc of the Sun, each with a different velocity vector. We derive projected morphologies of all clouds and estimate the volume filling factor of warm partially ionized material in the LISM to be between $\sim$5.5% and 19%. Relative velocities of potentially interacting clouds are often supersonic, consistent with heating, turbulent, and metal depletion properties. Cloud-cloud collisions may be responsible for the filamentary morphologies found in $\sim\frac{1}{3}$ of LISM clouds, the distribution of clouds along the boundaries of the two nearest clouds (LIC and G), the detailed shape and heating of the Mic Cloud, the location of nearby radio scintillation screens, and the location of an LISM cold cloud. Contrary to previous claims, the Sun appears to be located in the transition zone between the LIC and G Cloud.

Subject headings: ISM: atoms — ISM: clouds — ISM: structure — line: profiles — ultraviolet: ISM — ultraviolet: stars

1. INTRODUCTION

In their now classical theoretical models for the interstellar medium (ISM), Field et al. (1969), McKee & Ostriker (1977), and Wolfire et al. (1995a, 1995b) assumed the ISM to be in thermal and steady state equilibrium. In these models, three stable regimes coexist in pressure equilibrium: the cold neutral medium (CNM) with temperature $T \geq 50$ K, the warm neutral (WNM) or ionized medium (WIM) with $T \sim 8000$ K, and the hot ionized medium (HIM) with $T \sim 1{,}000{,}000$ K. These models include heating by ultraviolet (UV) photons on grains and polycyclic aromatic hydrocarbon (PAH) molecules and cooling by various forbidden lines and the hydrogen Lyα line. These models do not include gas flows or predict the expected sizes of the various components. Given the low density of interstellar gas and the presence of supernovae and strong stellar winds, one expects that the gas will be far out of thermal and pressure equilibrium and be highly dynamic. Various reviews (e.g., Cox 2005; McCray & Snow 1979) discuss these issues and highlight the complexity of the ISM.

The Local Bubble (LB) is a region of low-density, presumably hot gas extending in all directions to hydrogen column densities $\log N(\text{H \sc{i}}) = 19.3$ (Lallement et al. 2003). Its shape is determined by the onset of significant column density of Na I, indicative of a cold gas shell surrounding the LB. Although the LB is irregular in shape, it extends to roughly 100 pc from the Sun. For our purposes, we consider the local interstellar medium (LISM) to consist of the hot, warm, and cold gas located inside the LB. The LISM gas has been shaped by the supernova explosions and winds of massive stars in the Scorpio-Centaurus association and ionized and heated by radiation from hot stars and the Galactic UV background (e.g., Berghöfer & Breitschwerdt 2002) and so should provide a useful test of interstellar gas properties in our Galaxy and the assumptions that underlie theoretical models of the ISM. We can now study the LISM in detail because the ground-level transitions of many neutral and ionized atoms present in the UV could be observed with the high-resolution spectrographs on the *Hubble Space Telescope* (*HST*). With resolutions as high as $R \equiv \lambda/\Delta\lambda = 100{,}000$ ($\Delta v = 3.0$ km s^{-1}), both the Goddard High Resolution Spectrograph (GHRS) and the Space Telescope Imaging Spectrograph (STIS) have obtained stellar spectra containing numerous interstellar absorption lines. As described below, these ultraviolet spectra, together with ground-based spectra in the Ca II H and K resonance lines, provide critical data for sampling the kinematic and physical properties of warm interstellar gas along 157 lines of sight.

The dynamical structure of the LISM has a direct influence on the structure of the heliosphere around our solar system and astrospheres surrounding other nearby stars. The extent of the heliosphere (astrosphere) is determined by the balance of momentum (ρv^2) between the outward moving solar (stellar) wind and the surrounding ISM. Long-term variations in the solar wind strength are not well known, but observations of astrospheres around young solar analogs provide clues as to what kind of wind the Sun had in its distant past. The solar wind 3.5 billion years ago may have been $\sim$35-fold stronger than it is today (Wood et al. 2005a). In contrast, density variations spanning 6 orders of magnitude are commonly observed throughout the general ISM. However, variations in the dynamical properties of the surrounding ISM can also cause significant variations in the structure of the heliosphere even between clouds with little to no density variation. Reviews of heliospheric modeling include Zank (1999) and Baranov (1990), and the detection of astrospheres around nearby stars is reviewed by Wood (2004). Müller et al. (2006) explore the response of heliospheric models to various interstellar environments that exist in the LISM. Significant heliospheric (or astrospheric) compression

---

[2] Department of Astronomy and McDonald Observatory, University of Texas, Austin, TX 78712-0259; sredfield@astro.as.utexas.edu.
[3] Hubble Fellow.
[4] JILA, University of Colorado and NIST, Boulder, CO 80309-0440; jlinsky@jila.colorado.edu.

can impact planetary albedos, atmospheric chemistry, and biological mutation rates. Reviews of the implications of heliospheric variability are discussed by Redfield (2006) and Frisch (2006).

Crutcher (1982) noted that interstellar gas in the LISM flows in roughly the same direction away from the center of the Scorpio-Centaurus association. Lallement & Bertin (1992) then showed that the flow of interstellar gas in the direction away from the Galactic center is consistent with a vector that differs somewhat from that of the gas in the Galactic center direction. They coined the term AG Cloud for the former and G Cloud for the latter. The AG Cloud is now called the Local Interstellar Cloud (LIC), since the Sun has been presumed to be located just inside the LIC on the basis that the velocity of neutral helium flowing into the heliosphere is consistent with the LIC flow vector (Witte et al. 1993). Lallement et al. (1995) argued that the LISM has a complex velocity structure with at least seven clouds located within 12 pc. Using a larger data set, Frisch et al. (2002) were able to identify seven clouds in the LISM on the basis of their kinematics. Using Na I spectra of stars in the Galactic anticenter hemisphere, Génova & Beckman (2003) identified eight clouds of presumably cold gas lying beyond 50 pc of the Sun with velocity vectors very different from those identified in this paper. These clouds may lie at the edge of the LB or beyond.

The present work expands on the earlier studies in two ways. First, we analyze a much larger data set consisting of 270 individual velocity components along 157 lines of sight through the LISM. Each velocity component provides kinematical information (i.e., radial velocity) of a parcel of gas that we can analyze together with other velocity components to identify velocity vectors and morphologies of different gas clouds. Second, high-resolution GHRS and STIS spectra for 55 of these velocity components allow us to measure the widths of absorption lines from atoms and ions of different atomic weight to determine the temperature and turbulent velocity (Redfield & Linsky 2004b), and for 65 of the velocity components D I (an excellent proxy for H I in the LISM; Linsky et al. 2006) is observed together with other ions that can be used to calculate metal depletions (e.g., Redfield & Linsky 2004a). These measurements allow us to determine some of the physical properties of the clouds in addition to their kinematical and morphological properties.

In this paper we use the term "cloud" to refer to a contiguous parcel of interstellar gas inside the LISM with homogeneous kinematical and physical properties. We determine the morphology of 15 such clouds (§§ 2.3 and 3) by assuming that the interstellar gas flow inside each cloud is coherent and that the clouds have sharp edges. An upper limit to the distance of each cloud from the Sun is the distance to the nearest star whose spectrum shows a velocity component consistent with the cloud's velocity vector. We identify locations on the sky of possible cloud-cloud interactions and check whether these locations are consistent with other phenomena (§ 5). In subsequent papers we will describe how these cloud-cloud interactions could explain radio scintillation screens and the locations of cold clouds. The results may be used to test assumptions of sharp cloud boundaries and departures from coherent flow and to search for evidence of shear, cloud rotation and expansion, and alignment with magnetic fields (Cox & Helenius 2003).

2. DATA ANALYSIS

2.1. *Construction of LISM Observational Database*

The ability to assign large-scale dynamical flows to observed projected radial velocities requires an extensive and densely sampled observational database. We have compiled the most comprehensive high spectral resolution observational database from absorption-line transitions in the UV observed by *HST* and from the Ca II optical transition observed from the ground. Transitions in the UV are the most sensitive to the warm partially ionized clouds that populate the LISM, while Ca II is the transition most sensitive to warm gas in the visible (Redfield 2006). Only six sight lines have both UV and Ca II interstellar absorption detections: α Aql, α PsA, δ Cas, η UMa, α Gru, and ϵ Gru (see references in Redfield & Linsky 2002). Not all UV velocity components are detected in Ca II, but those that are agree in observed velocity very well. The absorption observed toward α Gru provides the only example where the ultra–high-resolution Ca II observations resolve multiple components from absorption identified as a single UV component (Crawford & Dunkin 1995; Redfield & Linsky 2002). About 26% of the sight lines are observed in several ions. Multiple-ion observations of the LISM along the same line of sight provide independent projected velocity measurements and provide additional diagnostics of the physical properties of the material (depletion, temperature, ionization, etc.). Even though only one to three velocity components are identified per sight line, moderately high spectral resolution is required to adequately separate and resolve individual absorbers with similar projected velocities.

Our database, which includes 270 individual velocity components along 157 sight lines, is derived from (1) the complete high-resolution UV database of *HST* observations of LISM absorption toward stars within 100 pc (see Redfield & Linsky 2002, 2004a and references therein), which represents 55% of the velocity components in our sample; (2) the high-resolution Ca II absorption measurements toward stars within 100 pc (Frisch et al. 2002; Redfield & Linsky 2002 and references therein), which represent 32% of the components in our sample; and (3) the moderate-resolution UV database of *HST* observations of LISM absorption toward stars within 100 pc (Wood et al. 1996, 2000, 2005b), representing the remaining 13% of the components in our sample. Physical parameter measurements (i.e., temperature, turbulent velocity, depletions) are available for 90 components, or one-third of the sample.

All absorption is assumed to be caused by the LISM. Contamination of the absorption database by absorption caused by edge-on circumstellar disks, although possible, is highly unlikely. Not only are nearby stars with circumstellar material rare, but the requirement of an edge-on orientation further limits the likelihood of observing such systems. Only a handful of such systems, which show circumstellar absorption, are known within 100 pc. The most prominent example is β Pic, whose spectrum shows stable absorption at the stellar rest frame and variable absorption components, both due to circumstellar gas (Hobbs et al. 1985; Brandeker et al. 2004), in addition to an LISM component, resolved from the circumstellar material only in the heaviest (i.e., narrowest) ions, such as Fe II (Lallement et al. 1995; Redfield & Linsky 2002). Only two other stars in the LISM database have known edge-on circumstellar disks: (1) β Car (Lagrange-Henri et al. 1990), in which only the Na I absorption feature was observed to vary, whereas the Ca II absorption is relatively steady and matches the UV observations (Redfield et al. 2007; Redfield & Linsky 2002); and (2) AU Mic (Kalas et al. 2004), which shows no circumstellar absorption in H_2 (Roberge et al. 2005; France et al. 2007) or other UV lines, including Lyα (Wood et al. 2005b), and the single UV observation does not allow for any constraint on the constancy of the observed absorption (Redfield & Linsky 2002). Therefore, we have retained these absorption features in the LISM database, but their removal does not significantly change the velocity vectors determined for the clouds for which they are members.
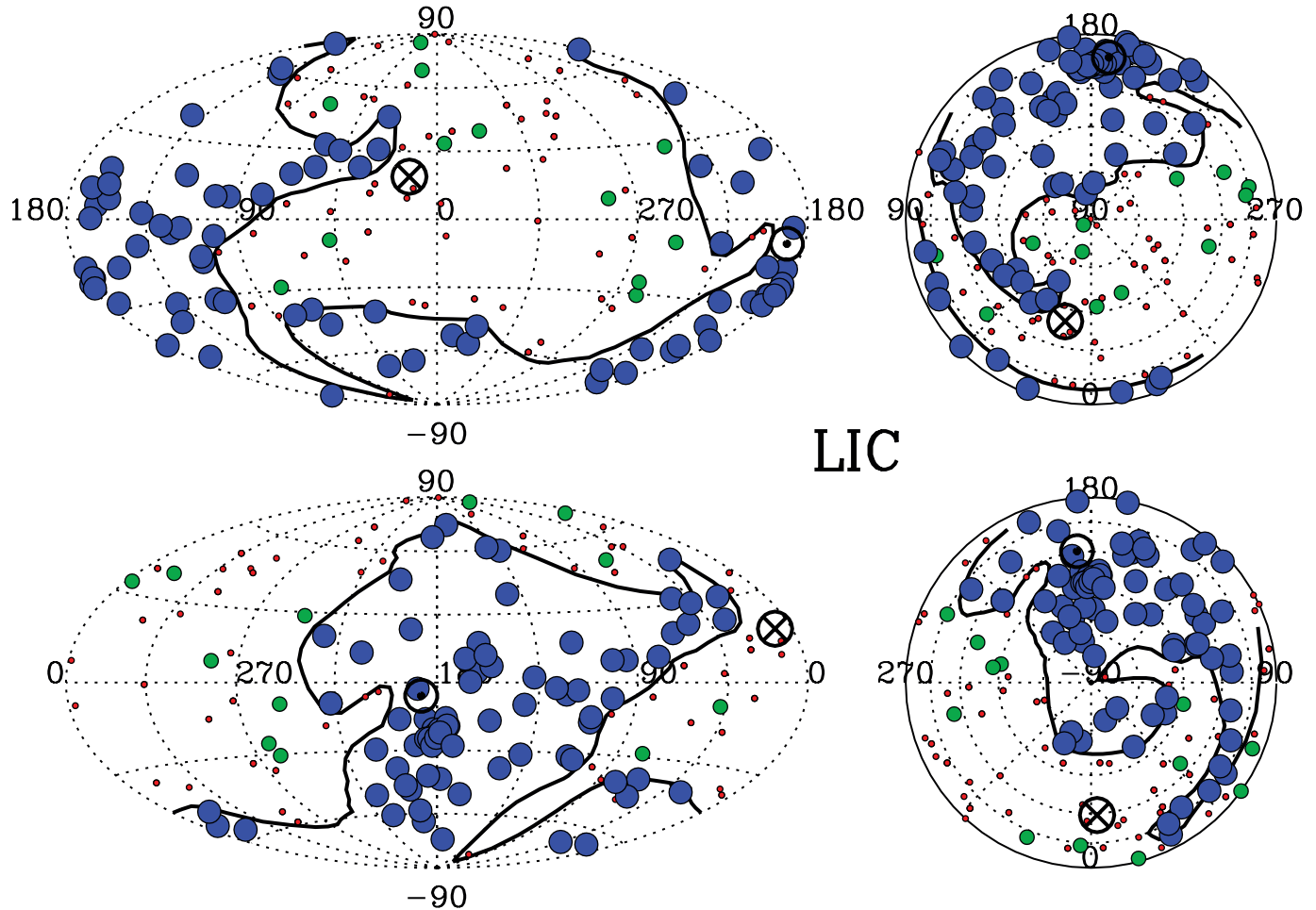
Fig. 1.—Four projections of the LIC boundaries in Galactic coordinates. All sight lines used in our analysis are displayed. The large blue circles indicate sight lines used to calculate the LIC velocity vector. The medium-sized green circles indicate sight lines with projected velocities that are consistent with the estimated vector but are considered part of another cloud (see § 2.2), while the small red circles indicate lines of sight that are inconsistent with the calculated velocity vector. The boundaries of the LIC are drawn to encompass all consistent sight lines (i.e., blue circles), while avoiding all other lines of sight (i.e., red and green circles). The upwind heliocentric direction of the velocity vector is indicated by the circled cross, while the downwind heliocentric direction is indicated by the circled dot. The four projections from upper left and moving counterclockwise are as follows: a Hammer projection of Galactic coordinates with the Galactic center in the middle, a Hammer projection of Galactic coordinates with the Galactic anticenter in the middle, a Lambert projection from the south Galactic pole, and a Lambert projection from the north Galactic pole.

We focus on using Ca II because it primarily traces warm LISM gas, whereas Na I primarily traces cold gas not common in the LISM. However, Na I is occasionally detected in absorption toward nearby stars (e.g., Blades et al. 1980; Vallerga et al. 1993; Welty et al. 1994; Welsh et al. 1994). Approximately one-third (49/157 = 31%) of the sight lines in our sample also have Na I observations, of which LISM absorption is detected along only 16 lines of sight. About one-half of the Na I detections are toward stars within 50 pc, so although relatively uncommon within 100 pc, Na I absorption is not significantly dominated by the cold gas located near the edge of the LB (Lallement et al. 2003). Therefore, a Ca II absorption component that is associated with a Na I component at the same velocity is not necessarily indicative of distant gas. Practically all LISM Na I absorption components have companion absorption components in Ca II at the same velocity, which indicates that the cold gas detected by the Na I absorption is physically associated with the warm gas detected by the Ca II absorption, and not separate clouds at coincident velocities. It appears that much of the cold gas in the LISM is associated directly with warmer gas and these structures share a common velocity vector.

Our combined database samples the sky unevenly because the sight lines were often selected to observe UV-bright stars or for

purposes other than measuring LISM absorption. Although this is the densest sampled UV/optical database of LISM absorption to date, there remain significant regions of poor sampling in both space and distance. The distribution of sight lines is shown for all of our dynamical cloud structures in Figures 1–15. The various symbols used to signify the sight lines, as well as a discussion of the morphology of the derived clouds, are provided in § 3. The median angular distance from one sight line to its nearest neighbor is 6.6°, ranging from observations of binary stars with angular separations of ~10″ (e.g., α Cen A and B, α CMa A and B) to the poorly sampled region near $l = 137°$ and $b = 49°$ where the maximum nearest neighbor separation is 21.5°. Areas of poor sampling limit our ability to detect dynamical cloud structures, as many sight lines through the same collection of gas are required to determine an accurate velocity vector. Poor sampling also limits our ability to estimate distances to structures in these regions.

2.2. Criteria for Identifying an Interstellar Cloud

We began our search for identifiable structures in the LISM with the properties of the LIC as our prototype. As shown by Lallement & Bertin (1992) and Redfield & Linsky (2000), the LIC moves as if it were a rigid structure, that is, the observed radial velocities toward nearby stars over a wide range of Galactic coordinates are consistent
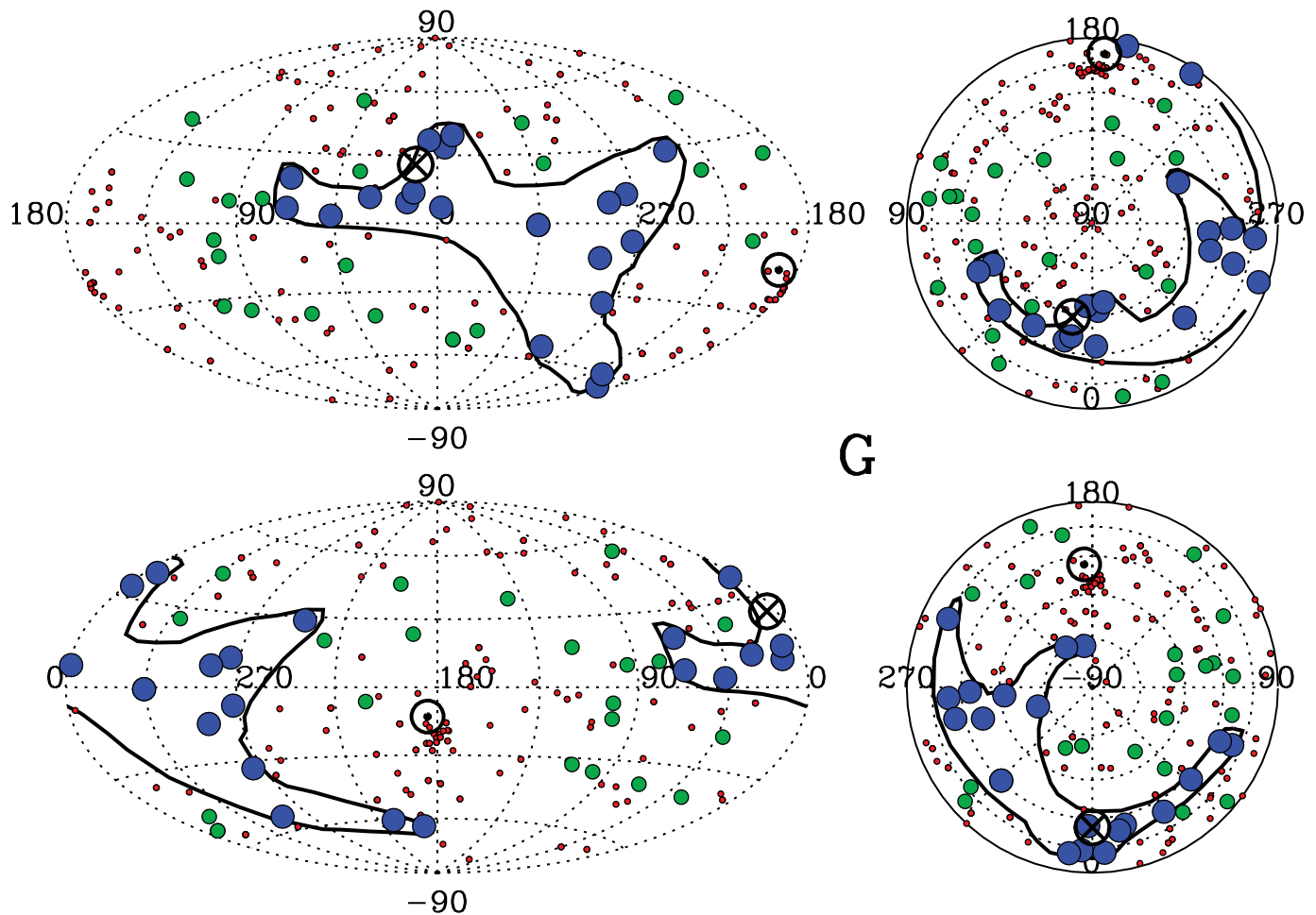
Fig. 2.—Same as Fig. 1, but for the G Cloud.

with a single velocity vector. The scatter of the measured radial velocities about the mean vector is generally less than 1 km s^{-1}, which is similar to the absolute velocity precision of STIS echelle data. Redfield & Linsky (2000) constructed a three-dimensional model for the LIC based on absorption-line data for 32 lines of sight. The edge of the cloud was determined by the measured H I column density along each line of sight and the assumption that the H I number density is the same throughout the LIC. This simple assumption cannot be readily tested and could be far from the truth. Thus, the true shape of the LIC is not well determined and the question of its edge, whether it be sharp or gradual, is unknown. Although Redfield & Linsky (2000) concluded that the LIC is roughly spherical in shape, the shape of interstellar clouds often appears to be filamentary based on an abundance of observations of nearby (Frisch & York 1983) and distant (e.g., Graham et al. 1995) filamentary structure in the ISM, presumably organized by magnetic fields (Jackson et al. 2003). We have therefore not assumed any a priori shape for the clouds in the LISM. In practice, we have followed a few simple rules in identifying interstellar clouds. Figures 1–15 show the spatial distribution and projected boundaries of the resulting dynamical clouds, and Tables 1–15 list sight-line membership of the clouds.

1. We determine the three-dimensional heliocentric velocity vector (three free parameters: the velocity magnitude [V_0] and the direction in Galactic coordinates [l_0, b_0]) that best fits the radial velocity database, where $V_r = V_0[\cos b \cos b_0 \cos (l_0 - l) + \sin b_0 \sin b]$. Here V_0 is >0 for downwind directions and <0 for upwind di-

rections. The first application of this procedure to the entire database yields a velocity vector consistent with absorption due to the LIC. Since LIC absorption is seen over much of the sky, the LIC should have the greatest number of observed sight lines and dominate the dynamical fit of the entire database. We next delete the velocity component that most significantly disagrees with the predicted projected velocity for LIC absorption and then recompute the velocity vector that best fits the remaining points. This procedure is continued until a satisfactory fit to the data is derived. Our criterion for ending the iteration process is that the removal of the next most discrepant data point does not significantly reduce the goodness-of-fit measure, χ_ν^2, as determined using the F-test, where $\chi_\nu^2 \equiv \chi^2/\nu$, ν are the number of degrees of freedom, and $\chi^2 \equiv \sum\{[V_r(\mathrm{obs}) - V_r(\mathrm{pred})]/\sigma_{V_r(\mathrm{obs})}\}^2$ (Bevington & Robinson 1992).

2. The next step is to apply the requirement of contiguity: we assume that the LIC does not have any detached pieces that have acceptable radial velocities but cannot be sensibly connected to the rest of the LIC because there are lines of sight between the two regions that do not show radial velocities consistent with the LIC velocity vector. Because of the similarity of the different velocity vectors of LISM gas, coincident projected velocities of two or more dynamical structures are common. (Those sight lines that have components consistent with the vector but not spatially contiguous are displayed as medium-sized green circles in Figs. 1–15). Although limiting the definition of LISM clouds to spatially coherent structures may prohibit the identification of complex morphologies, it has the advantage of preventing the
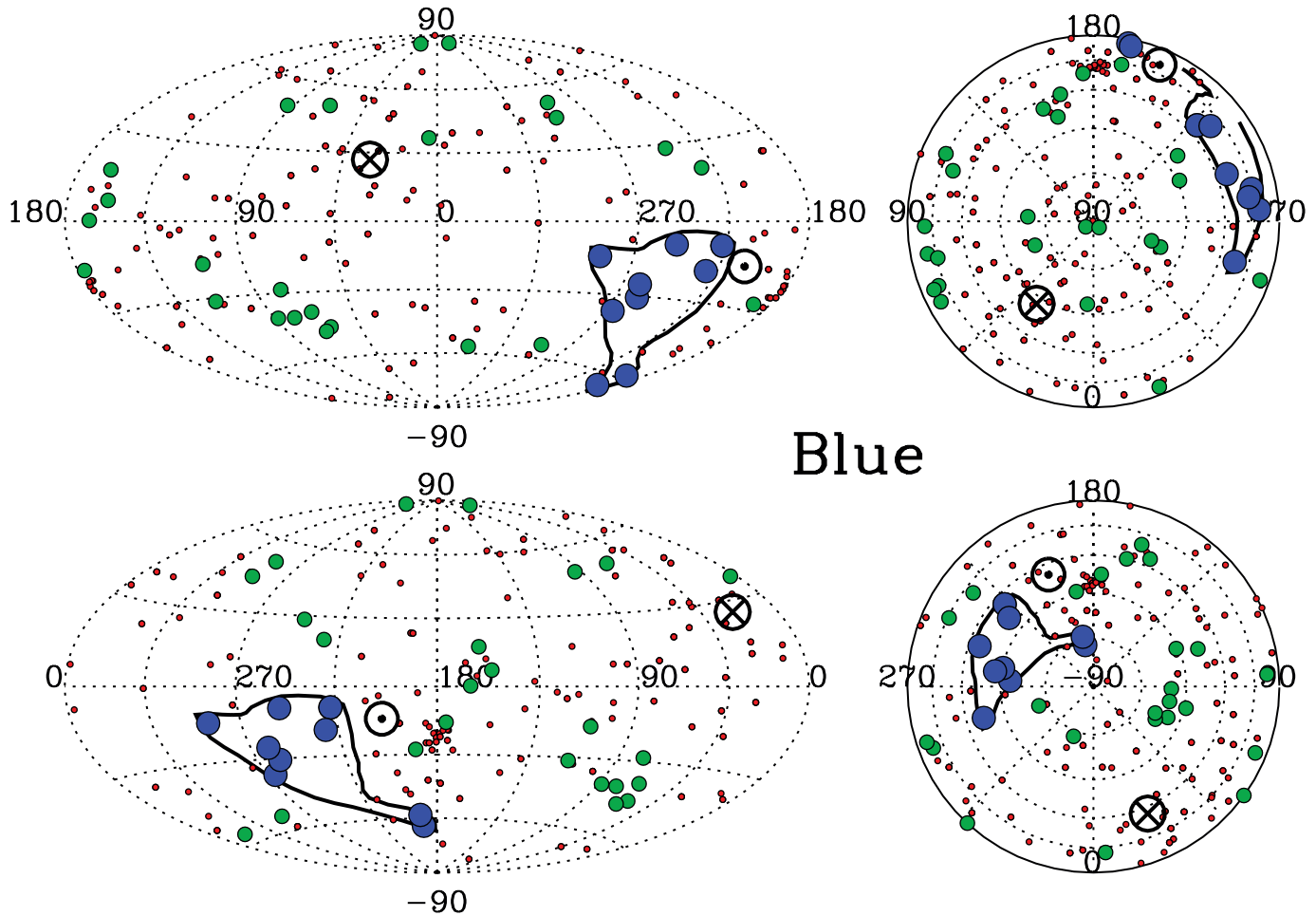
FIG. 3.—Same as Fig. 1, but for the Blue Cloud.

merging of distinct dynamical structures with similar velocity vectors. We draw a first approximation of the LIC shape (see Fig. 1) consistent with all data points lying within 1 σ of the predicted value if derived from high spectral resolution data and within 3 σ if drawn from the moderate-resolution data, with a contiguous morphology. We require at least four velocity components to constitute a distinct dynamical structure.

3. At this stage we reintroduce previously deleted velocity components that are consistent in velocity and continuity with the new vector. Particularly for the smallest clouds, some velocity components were prematurely removed from the fit at the earliest stages. In addition, it is at this point that other sight-line properties, if available, are compared in order to avoid assigning clearly different collections of gas with a coincidental velocity vector. When several cloud vectors predict a similar projected velocity for a particular sight line, we assign the velocity component to the cloud with the nearest neighboring line of sight that is uniquely a cloud member.

4. At this point, we have a nominal assignment of sight lines to a particular dynamical cloud. An iterative reevaluation of sight-line membership of previously determined dynamical clouds is performed and occasionally a reassignment of cloud membership is made, although this was relatively rare. The process is then repeated for the remaining unassigned velocity components. This iterative velocity vector technique is most successful at identifying clouds comprised of a large number of components (e.g., LIC and G Cloud) that subtend large angles on the sky (e.g., NGP

and Mic Clouds) or are significantly different dynamically than the average LISM flow (e.g., Blue and Aql Clouds). However, it has difficulty identifying compact dynamical clouds defined by only a handful of sight lines. In order to search for these kinds of clouds, we began the process with a preselected subset of sight lines that either are spatially grouped in a region without an identified dynamical cloud or have a common velocity difference from the general LISM flow, a technique used by Frisch et al. (2002). Those that produced a satisfactory velocity vector and survived the constraint of continuity resulted in the identification of some of our smallest clouds (e.g., Dor and Oph Clouds).

2.3. Collection of Warm Nearby Interstellar Clouds

We were able to fit rigid velocity vectors for 15 clouds in the LISM.[5] Absorption component membership and properties are given for each cloud in Tables 1–15, and the velocity vectors and goodness-of-fit metrics, χ^2_ν, are given in Table 16. The names of clouds are either historical (e.g., LIC: McClintock et al. 1978; G: Lallement & Bertin 1992; Blue: Gry et al. 1995; Hyades: Redfield & Linsky 2001; north Galactic pole [NGP]: Linsky et al. 2000) or based on constellations that dominate the area of the sky coincident with the cloud location. The sight-line members are listed in order of distance to the target star, along with the

---

[5] Projected and transverse velocities can be calculated for any sight line at http://cobalt.as.utexas.edu/~sredfield/LISMdynamics.html.
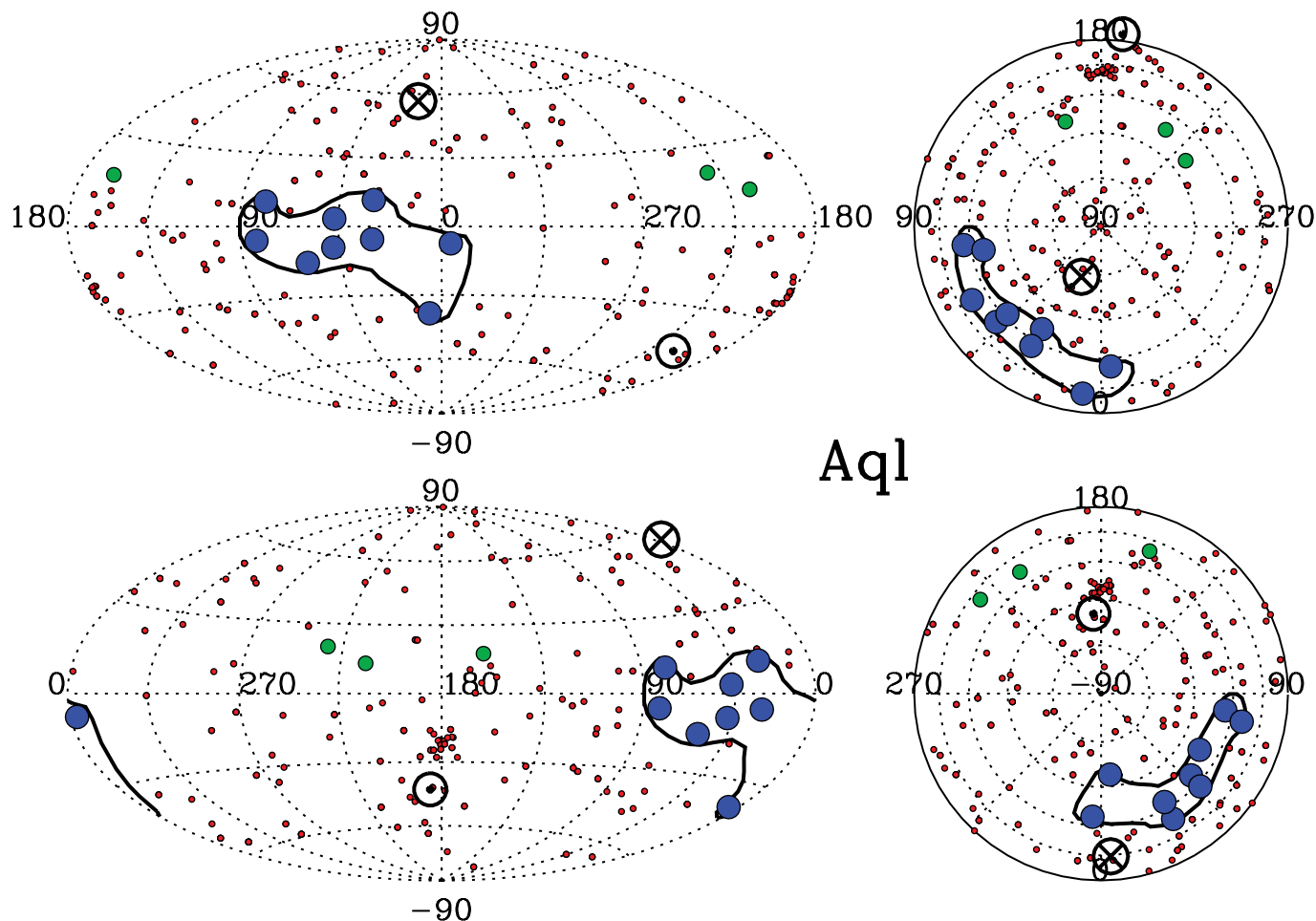
F_{IG}. 4.—Same as Fig. 1, but for the Aql Cloud. Note the small number of coincident velocities (i.e., green medium-sized circles). The Aql Cloud velocity vector is significantly different than the average LISM flow but successfully characterizes nine closely spaced sight lines.

observed projected velocity of LISM absorption, the deviation (σ) from the predicted projected velocity of LISM absorption, any other LISM properties along the line of sight [e.g., $N(\mathrm{H\,I})$, T, ξ, $D(\mathrm{Fe})$, and $D(\mathrm{Mg})$], and a list of other LISM clouds that could possibly explain the observed absorption component. The deviation between the observed and predicted projected velocity is given as $\sigma = (|v_0 - v_\star|)/\sigma_v$, where v_0 is the predicted projected velocity of absorption, $v_\star$ is the observed velocity, and σ_v is the error in the observed velocity, where we have imposed a minimum σ_v of 1 km s^{-1} for all high-resolution data and a minimum σ_v of 3 km s^{-1} for all medium-resolution data. The list of other clouds that could possibly explain the observed absorption component was required to meet slightly relaxed constraints from those imposed for cloud membership, such that those clouds listed in the last column of Tables 1–15 are within 10° of the sight line and predict a projected velocity within 3 σ of the observed velocity.

Three clouds, NGP, Oph, and Cet, have $\chi_\nu^2 > 3$, indicating a relatively poor match between our rigid velocity vector and the observed projected velocities. We believe that the high χ_ν^2 values for these clouds indicate departures from the assumption of rigidity rather than the existence of several cloudlets with very similar velocity vectors. For example, the NGP and Oph Clouds are relatively compact collections of many sight lines, 15 and 6, respectively, which supports a genuine connection between the absorbing material despite the poor fit to a rigid velocity vector. Likewise, although the Cet Cloud is filamentary and comprised

of only five sight lines, its high velocity makes it unlikely that a set of random velocities, for a contiguous group of sight lines, would all be consistent with such an extreme velocity vector.

The distributions of velocity amplitude (V_0) and direction in Galactic coordinates (l_0, b_0) for the 15 clouds are given in Figure 16 both in the solar rest frame (heliocentric) and relative to the local standard of rest (LSR). The vector solutions for all clouds have similar directions, suggesting that there is a common history or dynamical driver for all the warm LISM clouds, but there is a wide range of velocity amplitudes, suggesting the presence of shocks in the LISM (see McCray & Snow 1979). In particular, five clouds have velocity components that differ significantly from the mean value: the Blue and Hyades Clouds have $V_0 < 15$ km s^{-1}, and the Aql, Dor, and Cet Clouds have $V_0 > 50$ km s^{-1}.

Figure 17 shows the projections of the three-dimensional velocity vector solutions along different Galactic axes. The location of the center of each vector is placed in the direction of the center of the cloud at the distance of the closest star with the cloud's absorption velocity. This figure likewise demonstrates that the 15 velocity vectors are all variations on the same theme, in that they all are aligned in approximately the same direction; however, significant differences do exist between individual velocity vectors.

About 18.8% of the velocity components in our database cannot be assigned to any of our 15 derived velocity vectors. All unassigned components are listed in Table 17. Many of these velocity components may represent more distant LISM clouds that subtend smaller fractions of the sky and are probed by too few
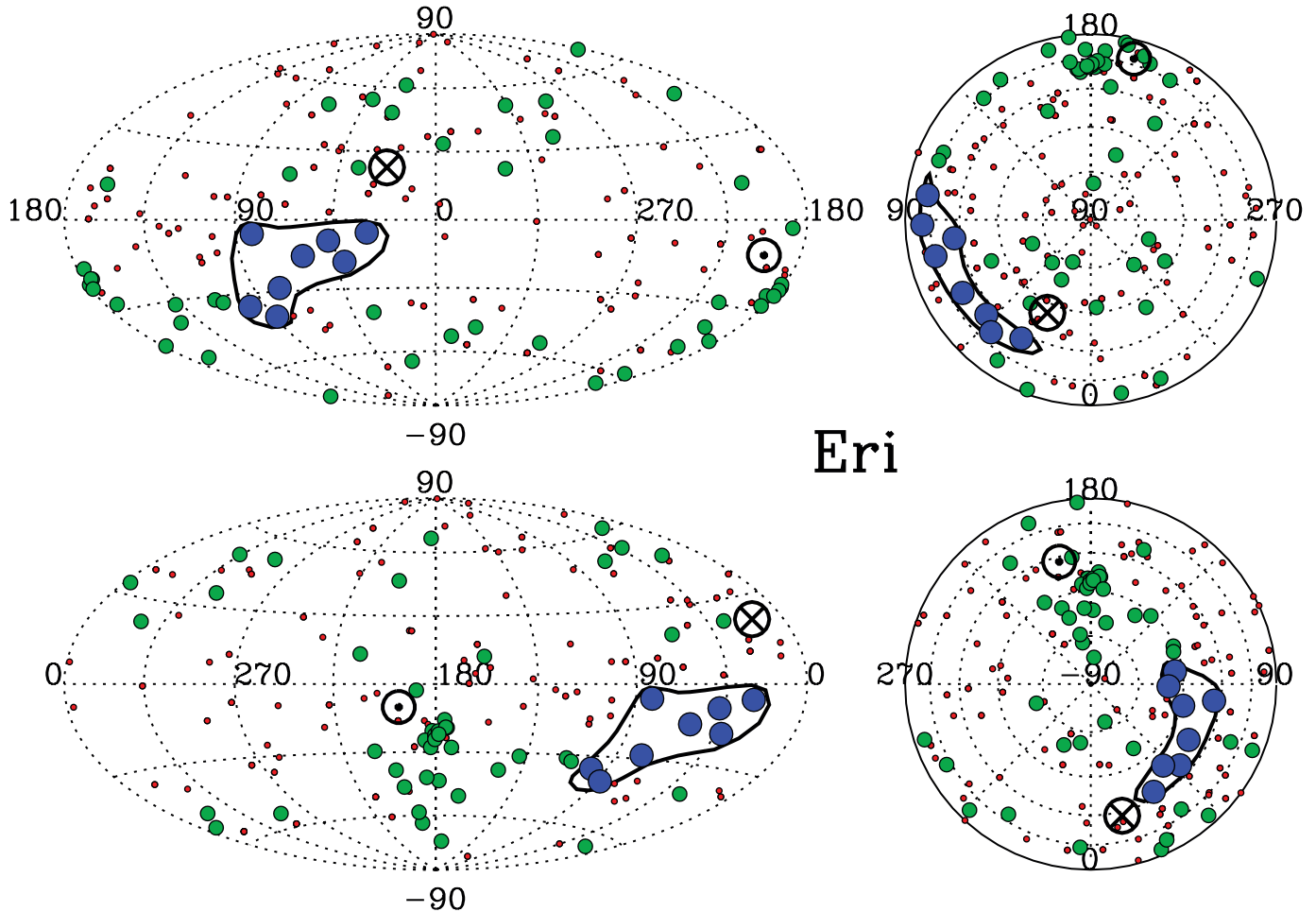
Fig. 5.—Same as Fig. 1, but for the Eri Cloud.

sight lines to derive a unique velocity vector. Approximately 90% of the 51 unassigned absorbers are toward stars beyond 15 pc. Only five stars within 15 pc contain unassigned absorption components, and all have an unidentified absorption component in addition to absorption from identified nearby clouds.

The first attempt to fit a rigid velocity vector to absorption lines from nearby stars was made by Crutcher (1982). Seven stars that were presumed to be within 100 pc, and which were dominated by a single velocity component in moderate-resolution ($R \sim 80{,}000$) Ti II observations by Stokes (1978), were used to solve for a single LISM velocity vector, $V_0 = 28$ km s^{-1}, $l_0 = 205°$, and $b_0 = -10°$. Two of the seven stars turn out to have *Hipparcos* distances >100 pc, while four of the remaining five have high-resolution UV or Ca II observations and are included in our database. However, all of these stars show clear evidence for multiple components in high-resolution spectra. Although Crutcher (1982) was able to derive the general LISM flow direction, this work demonstrates that analysis of the dynamical structure of the LISM requires (1) high spectral resolution observations of ions sensitive to LISM material, (2) accurate distances to the background stars, and (3) a much larger number of sight lines to disentangle the complicated spatial and kinematic structure of local material.

A series of papers, including Lallement & Bertin (1992) and Lallement et al. (1995), used high-resolution ($R \sim 110{,}000$) Ca II observations and UV observations of Mg II and Fe II of ~16 stars to derive two rigid velocity vectors that encompassed significant areas of the sky. The velocity vectors were associated with the LIC, where they derive a solution of $V_0 = 25.7$ km s^{-1}, $l_0 = 186.1°$, and $b_0 = -16.4°$, and the G Cloud, with a solution of $V_0 = 29.4$ km s^{-1}, $l_0 = 184.5°$, and $b_0 = -20.5°$. The LIC and G Cloud velocity vectors that we derive from 5 times the number of lines of sight are similar (see Table 16). For the LIC, we calculated a heliocentric velocity vector with a magnitude of 23.84 ± 0.90 km s^{-1} flowing toward Galactic coordinates $l = 187.0° \pm 3.4°$ and $b = -13.5° \pm 3.3°$. Our LIC vector is within ~1 σ of the direction proposed by Lallement & Bertin (1992) but 1.8 km s^{-1} smaller in amplitude. Our G vector is almost identical to their previous determination. This agreement, derived from a much larger sample, demonstrates not only the reliability of the analysis but also the ability to derive accurate velocity vectors from a relatively small number of sight lines.

Frisch et al. (2002) derived a bulk flow vector, essentially the average velocity vector consistent with 96 velocity components from 60 stars within 132 pc. As we found with our larger database, the fit to all of the velocity components leads to a solution that approximates the LIC velocity vector, since LIC absorption dominates observations of nearby stars, although G Cloud absorption also contributes significantly. Frisch et al. (2002) assumed the direction of that bulk flow vector for all LISM clouds (except the LIC), then identified compact collections of absorbers that show common velocity magnitude departures from the bulk flow velocity. Our Blue Cloud vector, derived from 10 velocity components, matches well with that calculated by Frisch et al. (2002) from only two velocity components. However, the other cloud vectors
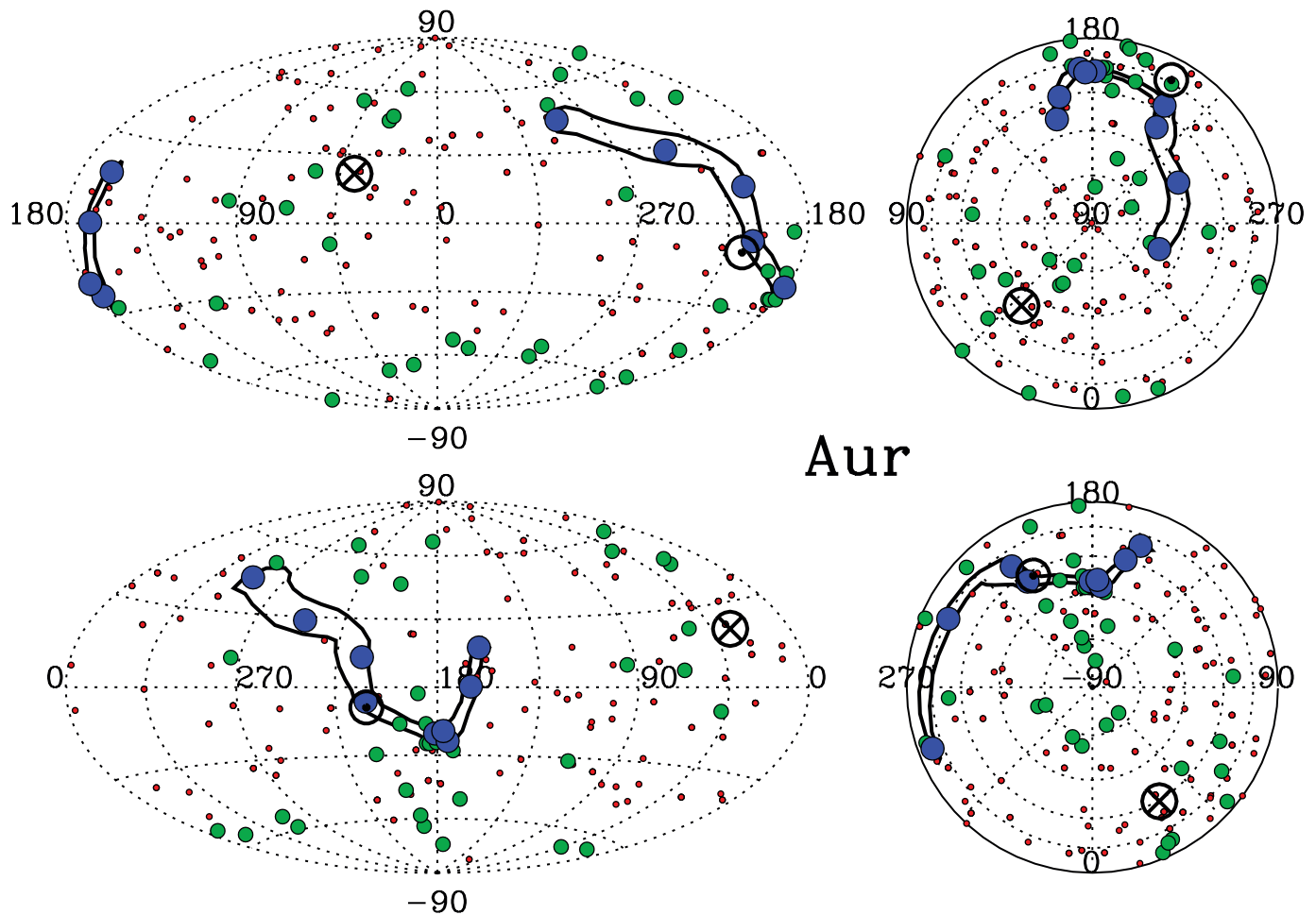
FIG. 6.—Same as Fig. 1, but for the Aur Cloud.

discussed by Frisch et al. (2002) are not obviously comparable to the vectors that we derive. In particular, the remaining clouds only differ from the bulk flow by $\leq 3\,\sigma$. Therefore, several of the velocity components identified in Frisch et al. (2002) are included as members of the LIC in our calculation. Although the directions of velocity components in the LISM are similar, the assumption that they are identical can hinder the identification of distinct dynamical structures.

In situ measurements derived from neutral helium (e.g., Witte 2004), pickup ions (e.g., Gloeckler et al. 2004), and backscattered UV emission (e.g., Vallerga et al. 2004; Lallement et al. 2004) provide information on the interstellar flow vector that our solar system is presently encountering. Möbius et al. (2004) summarize the results of these experiments and provide the weighted mean values for the flow vector, $V_0 = 26.24 \pm 0.45$ km s^{-1}, $l_0 = 183.4° \pm 0.4°$, and $b_0 = -15.9° \pm 0.4°$. Although technically this vector is consistent within $3\,\sigma$ of both the LIC and G Cloud vectors, the in situ velocity is intermediate between the velocities of the LIC and G Cloud by 2.4 and $2.9\,\sigma$, respectively. Previous studies (e.g., Lallement & Bertin 1992) have concluded that the flow in the heliosphere is at the LIC velocity. Redfield & Linsky (2000) and others have argued that the solar system is located near the edge of the LIC and is moving toward the G Cloud. However, the new lower LIC velocity amplitude that we now derive suggests that the in situ measurements could be sampling an interaction region between the faster moving G Cloud material and the slower moving LIC material (see Table 16 and § 5.5). This conclusion is supported by the 6303 ± 390 K temperature

of interstellar gas in the heliosphere (Möbius et al. 2004), which, like the velocity, is intermediate between the temperature of the LIC gas (7500 ± 1300 K) and the G Cloud gas (5500 ± 400 K), although the differences have a lower significance of 0.9 and $1.4\,\sigma$, respectively. Additional temperature measurements, and therefore a refinement of the mean temperature, of both the LIC and G Cloud would be possible with observations of multiple ions along additional sight lines. Currently, such measurements are available along only 29 sight lines, 24 of which probe the LIC or G Cloud material (Redfield & Linsky 2004b). If the heliosphere is now located in a transition zone between the clouds, then we predict that long-term in situ measurements will gradually approach the G Cloud velocity and temperature.

3. MORPHOLOGY OF WARM CLOUDS IN THE LISM

Figures 1–15 show the morphologies of each cloud encompassing the sight lines consistent with the 15 rigid velocity vectors derived from the LISM database.[6] The sight lines utilized in the velocity vector calculations are indicated by the large blue circles, while sight lines with consistent projected velocities, but assigned to other clouds, are shown by the medium green circles, and those sight lines with observed projected velocities that are inconsistent with the velocity vector fit are indicated by the small red circles. The projected morphology of each cloud is drawn to

---

[6] Probable cloud membership, based on the projected cloud morphologies, can be calculated for any sight line at http://cobalt.as.utexas.edu/~sredfield/LISMdynamics.html.
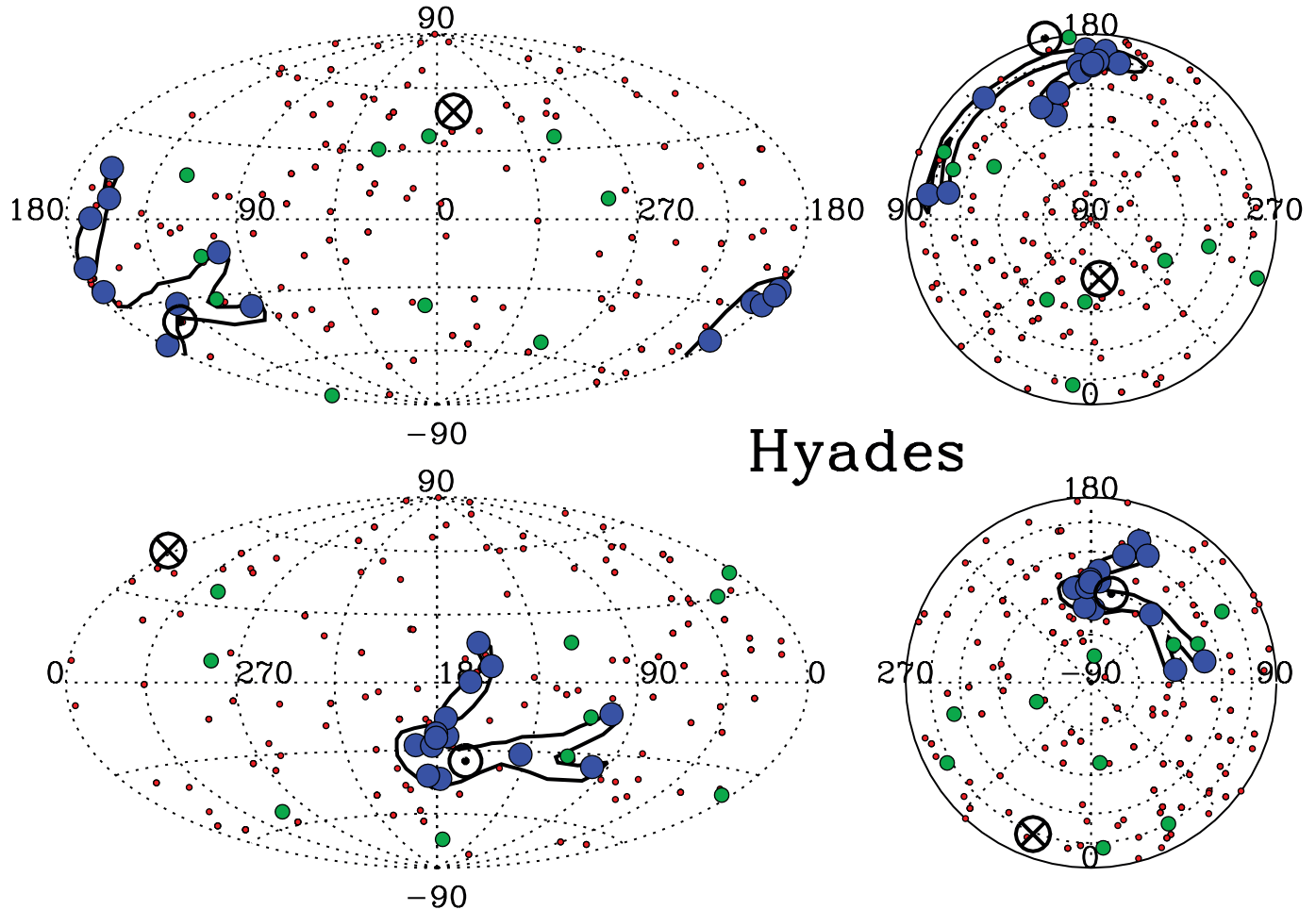
Fig. 7.—Same as Fig. 1, but for the Hyades Cloud.

include all sight lines used in the velocity fit, while avoiding all lines of sight that are inconsistent with the velocity vector. Each figure shows the cloud morphology from four different directions in Galactic coordinates.

Although the filamentary nature of the clouds could be exaggerated in some cases because of the low spatial sampling and our requirement of cohesion, approximately one-third of the clouds have projected morphologies that are clearly filamentary. It is possible that a couple of the "compact" morphologies may actually be filamentary but, due to a chance orientation, are projected as a compact cloud on the sky. However, it would be highly unlikely that the orientations of many "compact" clouds would be precisely aligned along the line of sight to hide the true morphology of the clouds. Determining the true morphology of these clouds, regardless of orientation, requires a database with high spatial *and* distance sampling. The orientations of the observed filamentary clouds are not similar, which argues against an association with a global magnetic field that may thread through the LISM. Instead, the filamentary regions, which generally trace the boundary between the LIC and G Cloud, may indicate regions of cloud-cloud interactions, where the rigid velocity structure is disrupted and potentially shocked by the collision of two adjacent clouds.

4. PHYSICAL PROPERTIES

Table 18 summarizes basic physical properties (e.g., coordinates of the cloud center, upper limits to the cloud's distance, projected surface area, weighted mean temperature, turbulent ve-

locity, and depletion of iron and magnesium) of the 15 clouds. The surface area on the sky is simply the surface area of the projected boundaries shown in Figures 1–15. The temperature and turbulent velocities are derived from comparisons of the measured Doppler widths of absorption lines of elements with different atomic masses (e.g., deuterium and iron) using the relation $b^2 = 2kT/m + \xi^2$ (Redfield & Linsky 2004b; Wood et al. 1996). The depletions, $D(X) = \log(X/H) - \log(X/H)_\odot$, are calculated using the Asplund et al. (2005) solar abundances, where the hydrogen abundance is typically calculated from D I and converted to H I using the remarkably constant LISM D/H ratio of $(1.56 \pm 0.04) \times 10^{-6}$ (Linsky et al. 2006). The depletions do not take into account partial ionization of hydrogen, which is likely important, or neutral or doubly ionized magnesium and iron, which are likely much less important since they are not expected to become a dominant ionization stage of either element (e.g., Slavin & Frisch 2002; Lehner et al. 2003). The weighted mean and 1 σ uncertainty of the mean are listed for all physical properties with measurements on multiple sight lines. No significant correlation appears to exist between any of the physical properties listed and cloud morphology. In the following discussion of physical properties of individual clouds, we consider only the nine clouds that have more than one sight line with physical measurements.

4.1. *Distance Limits*

Although a detailed look at the distances of the 15 LISM clouds is beyond the scope of this paper, we can immediately place distance constraints based on the distance of our background sources
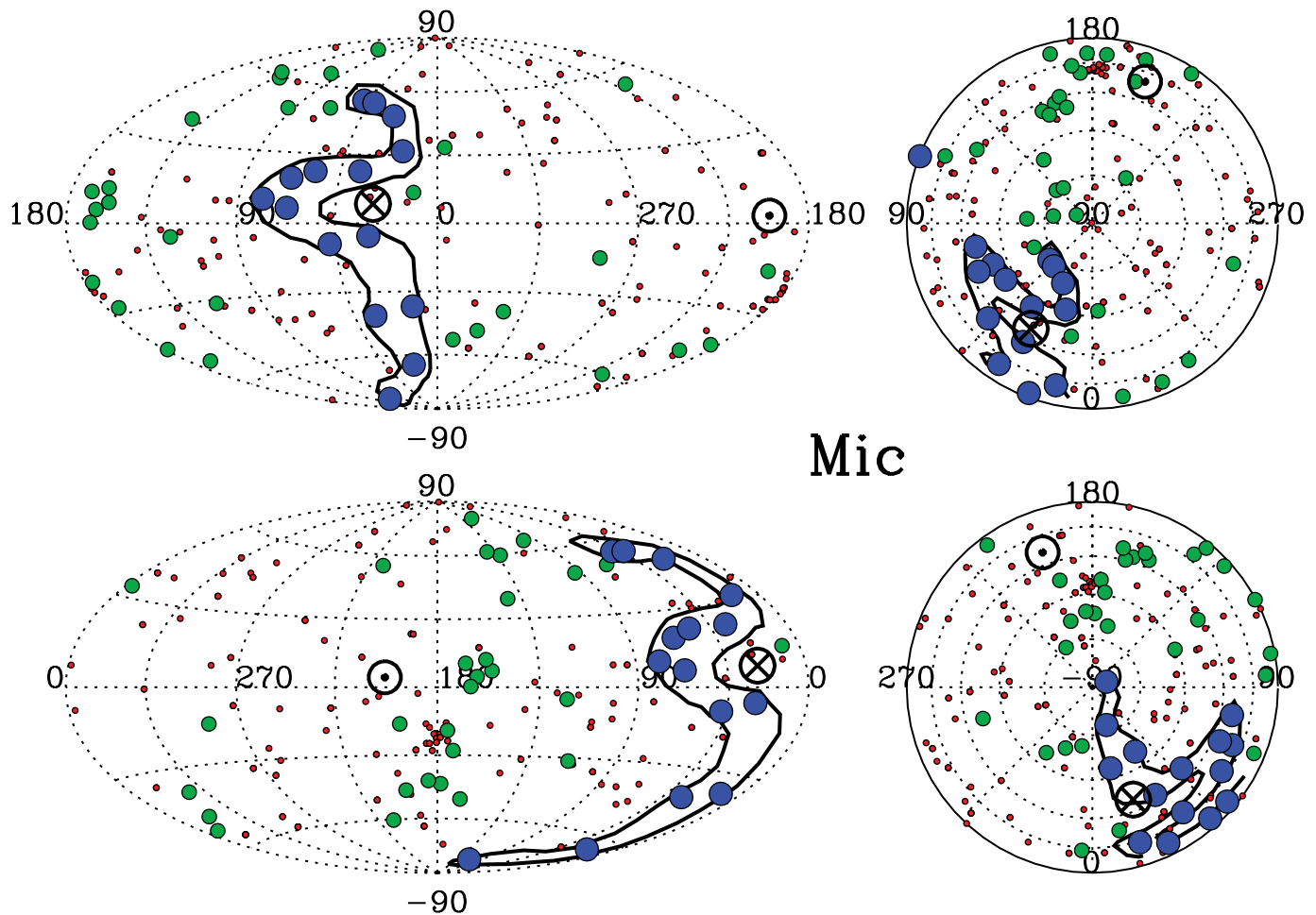
FIG. 8.—Same as Fig. 1, but for the Mic Cloud.

and provide some insight into the three-dimensional structure of the LISM. In Table 18 we list the distance of the closest star with absorption from the cloud, which provides an upper limit to the distance of the cloud. All of the clouds lie within 15 pc, and half lie within ∼5 pc, which is much smaller than the volume of the LB, but consistent with the large projected surface area that these clouds subtend. The distribution of many clouds with a range of dynamical properties in such a small volume makes collisions between clouds a real possibility. The implications of such interactions are explored in § 5.

Based on the distances of member sight lines, the G Cloud has a more stringent distance upper limit than the LIC. However, because the temperature and velocity of the interstellar material that is flowing into the solar system are consistent with early estimates of LIC material (Möbius et al. 2004), the Sun has been thought to actually be surrounded by the LIC (although see § 5.5 for a detailed discussion of this topic). Since LIC absorption is not observed in all directions (e.g., toward the Galactic center) and since the Sun is moving in roughly the direction of the Galactic center and the G Cloud (see Fig. 19 below), the heliosphere has been thought to be at the very edge of the LIC (Redfield & Linsky 2000).

4.2. Volume Filling Factor of the Warm LISM

We have not yet created a full three-dimensional morphological model of the LISM, but with a few assumptions and a simple toy model, we can estimate the volume filling factor of the warm

partially ionized gas in the LISM. First, we assume that all of the warm LISM material is located within 15 pc of the Sun. Although the LISM is often considered to be the volume of material within the LB, which extends out to roughly 100 pc in all directions, it seems that most of the warm material is located only a short distance from the Sun. This is shown, for example, in Figure 14 of Redfield & Linsky (2004a), where the average number of absorbers per unit distance levels off at a distance of ∼15 pc. No significant correlation exists between the observed line width or column density and the distance of the background star. Therefore, it is unlikely that unrecognized line blends along more distant sight lines are the cause of the observed leveling off of the average number of absorbers, but it is indicative of the true distribution of warm gas in the LISM. Based on Figure 14 of Redfield & Linsky (2004a), there are on average ∼1.7 absorbers per sight line. Therefore, the projected surface area of all LISM clouds should total ∼1.7(4π).

Initially, we assume that all of the warm LISM clouds are similar in size and density to the LIC. We assume that all warm clouds have a radius of 1.5 pc and a total hydrogen density of 0.2 cm^{-3}, obtained from measurements of the He I volume density streaming into the solar system from Gloeckler et al. (2004), the H I–to–He I ratio of the LISM from Dupuis et al. (1995), and the three-dimensional model of the LIC from Redfield & Linsky (2000). In addition, the assumed radius and density result in a full cloud hydrogen column density of ∼2 × 10^{18} cm^{-2}, which matches the typical observed hydrogen column density (Redfield & Linsky 2004a).
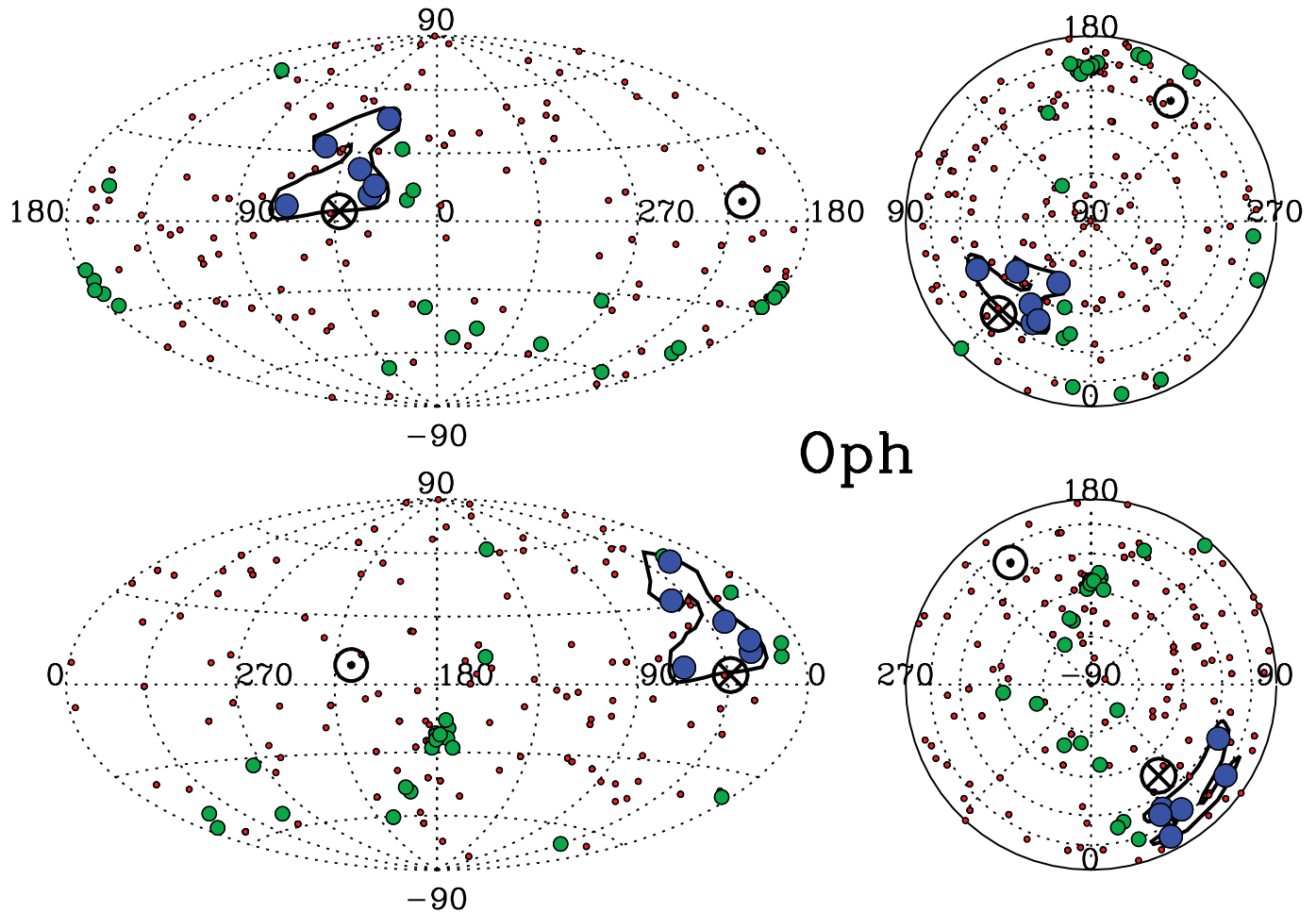
FIG. 9.—Same as Fig. 1, but for the Oph Cloud.

We ran 1000 simulations of cloud distributions, for a range of total warm clouds (n) in the LISM from $n = 1$ to 100 clouds, where all clouds were randomly centered at distances from 0 to 15 pc. Since clouds are not allowed to overlap, only one cloud can surround the solar system, that is, an LIC analog. In order to more closely match the model with the observed LISM, we have assumed the LIC projected surface area of 18,270 deg^2 for the LIC analog (see Table 18), instead of 41,250 deg^2. The remaining clouds' projected surface areas were calculated based on their size, geometry, and distance. In the spherical cloud scenario, the solution to an average of 1.7 absorbers per sight line leads to $\sim$55 clouds within 15 pc and a volume filling factor of warm partially ionized material of $\sim$5.5%.

We also ran a suite of simulations varying the geometry (i.e., ellipsoids with a range of aspect ratios from 1.33 : 1 to 10 : 1, both flattened [i.e., pancakes] and elongated [i.e., cigars]) and fraction of ellipsoid to spherical (which ranged from 0.3 to 1.0). The orientations of all clouds were determined randomly. Non-spherical geometries naturally lead to larger volume filling factors and fewer clouds, since a greater total volume can be produced with fewer clouds without necessarily increasing the projected surface area. The volume filling factors that resulted ranged from 5.5% to 19%.

Figure 18 compares the projected surface area distribution of our sample with two of our idealized simulations. The distribution of observed projected surface areas matches fairly well with that predicted for both the $\sim$55 spherical LIC-like clouds within

15 pc and a simulation of 35 clouds, half of which are ellipsoids with an elongated aspect ratio of 10 : 1. There is an observational bias toward detecting the nearest clouds with the largest projected surface areas. We restricted our dynamical cloud modeling to collections of gas that had at least four sight lines with which to determine a velocity vector.

About 18.8% of absorbers are not accounted for in our 15 cloud dynamical model of the LISM. The missing absorbers may represent detections of more distant and smaller projected surface area clouds. If we assume that we have detected all clouds with a log surface area >3.1 ($\sim$1260 deg^2), which is the lower limit of the LISM clouds with measured velocity vectors (see Table 18), we can estimate the number of sight lines that probe "undetected" clouds, or clouds with a log surface area <3.1 (see Fig. 18). Our toy models have 10.2–11.9 clouds with log surface area >3.1, slightly lower, but similar to the 15 observed clouds. The total projected surface area for all clouds with log surface area >3.1 ranges from 55,290 to 60,430 deg^2 in our simulations. This matches well the total projected surface area of the observed clouds (57,830 deg^2). With an estimate of the total projected surface area of "undetected" clouds and the assumption that all sight lines are uniformly distributed, we can predict the percentage of observed components that will be left over, after those associated with the large nearby clouds are removed. The percentage of unassociated velocity components in the simulations is between 14.5% and 21.5%, which matches closely the percentage of components in our database (18.8%) that are unassigned, which allows
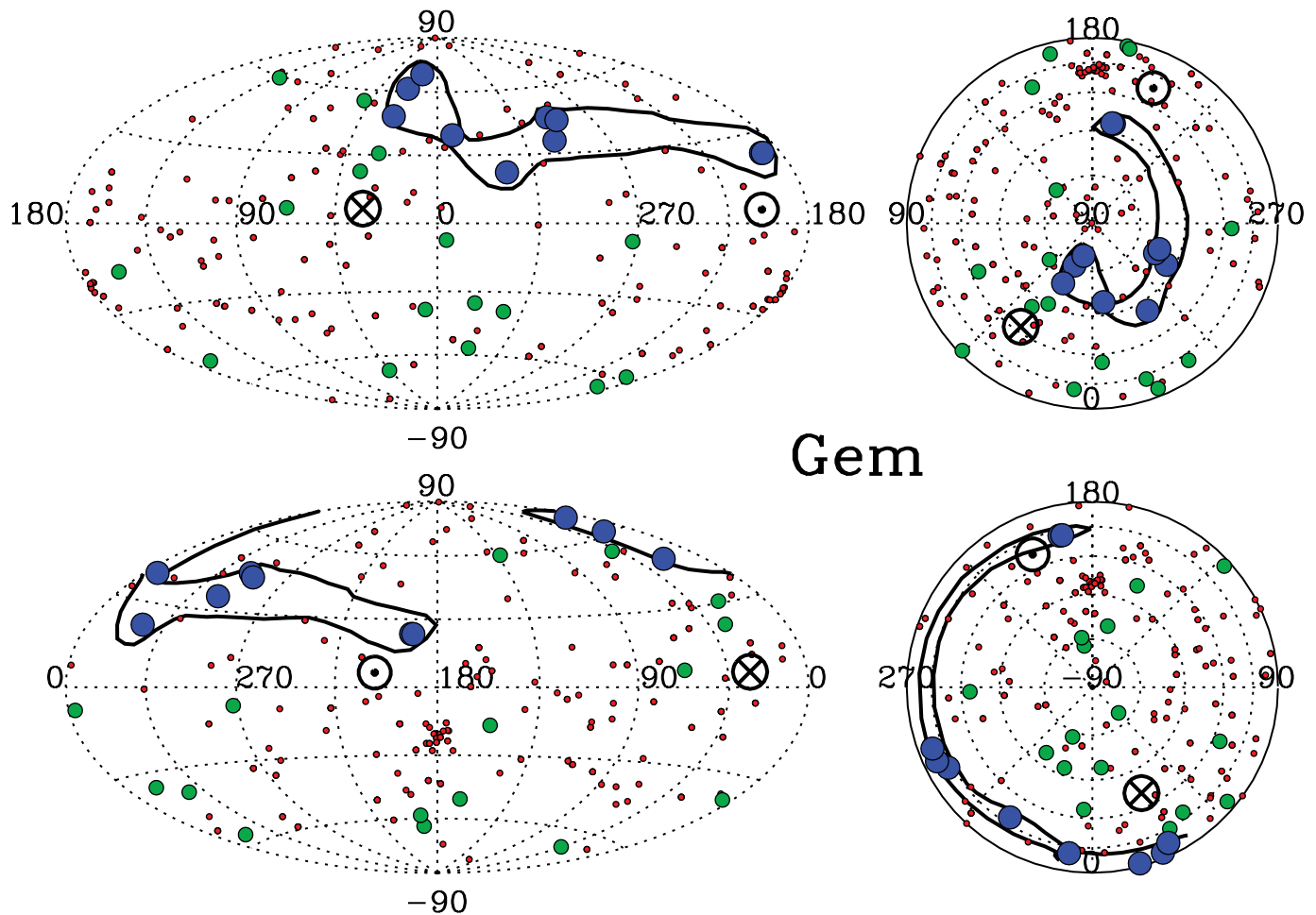
Fig. 10.—Same as Fig. 1, but for the Gem Cloud.

for the possibility that the absorbing material associated with these components is indeed located within ~15 pc, even though the background star is much farther away.

5. WHERE CLOUDS COLLIDE

5.1. *The "Ring of Fire" around the G Cloud*

Figure 19 shows the projected morphologies of all 15 clouds, which collectively cover more than 90% of the sky. The LIC and G Cloud clearly dominate the sky and contain large areas where one or the other is the only absorber along the line of sight. At the boundaries of the LIC and G Cloud, several overlapping absorbers are typically present, particularly near l from $40°$ to $80°$ and b from $-15°$ to $+30°$, as well as near l from $270°$ to $320°$ and b from $+20°$ to $+50°$ and from $-70°$ to $-30°$. These areas at the boundaries of the LIC and G Cloud may be dynamical interaction zones, which produce "new" clouds with significantly different kinematic properties. We refer to the active boundary of the G Cloud where the G Cloud and LIC may be colliding as the "Ring of Fire," in analogy to the Pacific Ocean "Ring of Fire" where dominant tectonic plates (here interstellar clouds) interact, resulting in a highly dynamic interaction zone that gives rise to earthquakes and volcanos (here interstellar shocks, heating, or turbulent flows).

One example of this interaction may be the Mic Cloud, whose morphology appears to mirror the adjacent sections of the LIC and G Cloud, as shown in Figure 20. At positive Galactic lat-

itudes, where the projected morphologies of the LIC, G Cloud, and Mic Cloud are coincident, the median predicted radial velocity difference between the LIC and G Cloud is ~5.5 km s^{-1}. The Mic Cloud may have been created by the faster G Cloud colliding with the LIC, which is moving ~5.5 km s^{-1} slower in the radial direction.

5.2. *Cloud Interactions, Turbulence, and Shocks*

Except for the LIC, many clouds have only three to five sight lines with measurements of physical properties, and six of the clouds have one or no sight lines with measured physical properties. As a result, it is difficult to explore the homogeneity or variation of properties across an individual cloud. Small-scale variations are not observed in the warm LISM clouds, based on identical absorption properties of nearby binary stars (e.g., α Cen A and B, Linsky & Wood 1996; Lallement et al. 1995; α CMa A and B, Lallement et al. 1994; Hébrard et al. 1999) and the lack of significant variation among a sample of 18 closely spaced Hyades stars, down to scales between 0.1 and 1 pc (Redfield & Linsky 2001). Therefore, we may expect that the physical properties of LISM clouds are relatively homogeneous, or at least slowly varying within a cloud.

Table 18 lists the weighted mean values of physical properties for all cloud members, as well as the weighted average standard deviation, which gives an indication of how tightly the values are scattered about the weighted mean. For example, D(Fe) in the LIC, even though there are 12 measurements, much more
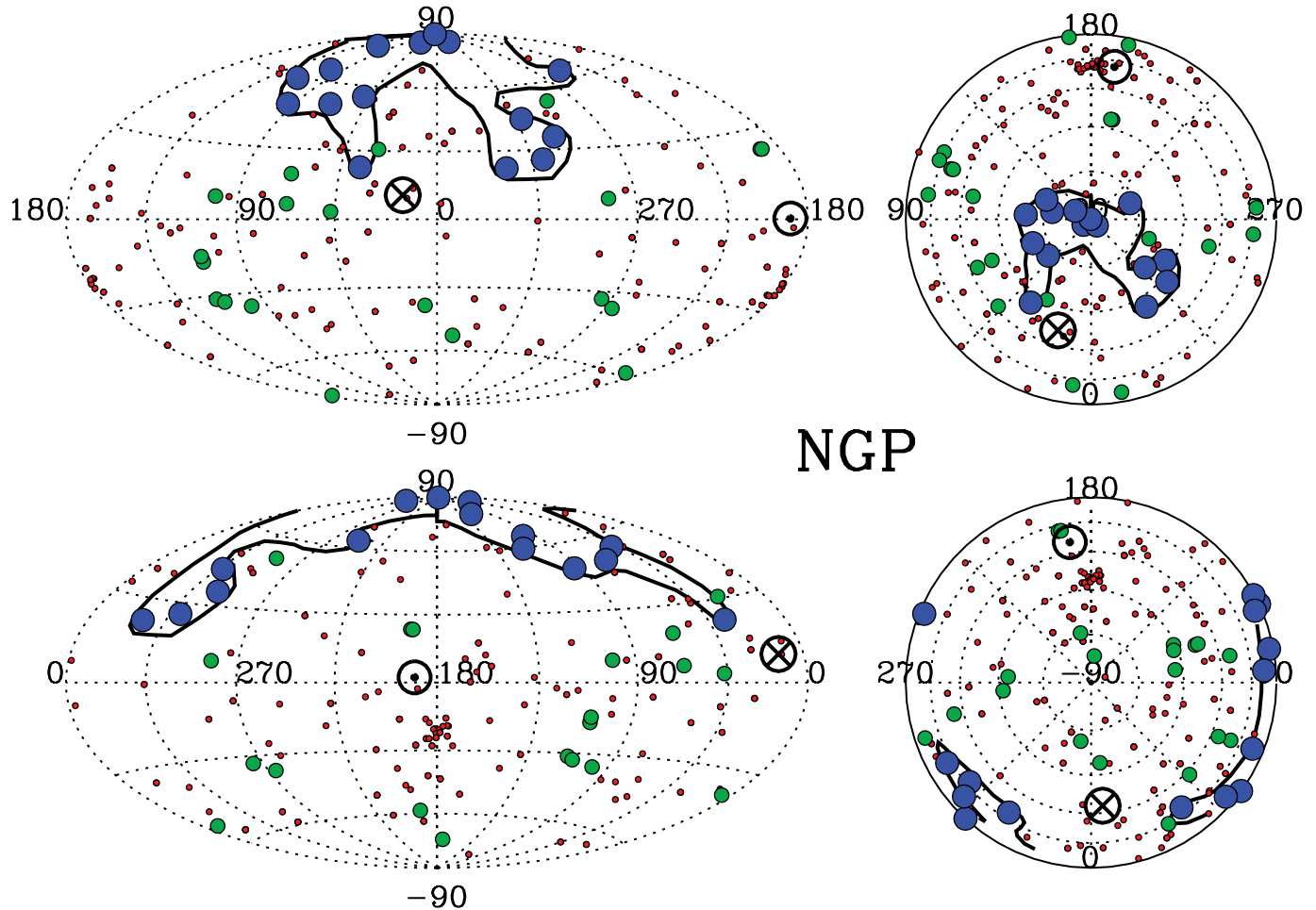
FIG. 11.—Same as Fig. 1, but for the NGP Cloud.

than any other cloud, has the lowest weighted average standard deviation, indicating that little variation is detected across the LIC. In contrast, due to the wide range of values in the Hyades and Mic Clouds, there is a large weighted average variance (although these clouds have only a few measurements). In particular, note the anomalous depletion measurement of G191-B2B associated with the Hyades Cloud (see Table 7). The ~ 8.6 km s^{-1} component, consistent dynamically and spatially with the Hyades Cloud, is detected in both low-ionization ions (e.g., D I, N I, O I, Mg II, etc.; Lemoine et al. 1996; Redfield & Linsky 2004a) and high-ionization ions (e.g., C IV; Vennes & Lanz 2001). The nature of the absorbing material along this line of sight is not well known, and the high-ionization material may be associated with nebular circumstellar material surrounding G191-B2B (Bannister et al. 2003). Although such contamination may be present along some sight lines in our sample, the need in this analysis to bring together a large number of independent LISM measurements aids in reducing and identifying anomalous data points. Indeed, the high weighted average standard deviation of depletion in the Hyades Cloud clearly identifies the G191-B2B sight line as anomalous. Henceforth, we assume that all measurements sample the physical properties of the LISM, although highly deviant data points may indicate interesting sight lines that require additional observations and further attention.

If we assume that we can estimate an individual cloud's mean properties by assuming that clouds are approximately homogeneous, then we can use the few available physical measurements to make a reasonable estimate of the cloud properties and to

search for possible correlations. For example, the Mic Cloud, already identified by its filamentary morphology and location at the boundary of the LIC and G Cloud, has the highest temperature ($\langle T \rangle = 9900$ K) and one of the highest turbulent velocities ($\langle \xi \rangle = 3.1$ km s^{-1}). These properties support the argument that the Mic Cloud is the result of the collision of the LIC and G Cloud.

The weighted mean depletions of iron [D(Fe)] and magnesium [D(Mg)] are plotted versus the weighted mean turbulent velocity (ξ) for the nine clouds in Figure 21. A clear correlation is evident. For iron, the linear correlation coefficient $r = 0.69$, and the probability (P_c) that this distribution could be drawn from an uncorrelated parent population is 1.7%, while for magnesium, $r = 0.73$ and $P_c = 1.2\%$.

The correlation of small depletions with high turbulence suggests that the destruction of dust grains has returned these ions to the gas phase. A possible alternative explanation is that, statistically, clouds with higher turbulence have higher percentage ionization of hydrogen, since the depletions were computed assuming that hydrogen is neutral. However, using the ionization model of the LIC produced by Slavin & Frisch (2002) taking the ionization of hydrogen, magnesium, and iron into account only produces a 0.05–0.10 decrease in the measured depletion. This adjustment is significantly less than the typical 1 σ error for the weighted mean depletion for individual clouds, and much less than the ~ 1 dex variation seen over all LISM clouds. Therefore, since we currently have no evidence for a correlation between turbulence and ionization structure and the depletion adjustment using LIC ionization models is small, we consider here possible dust destruction
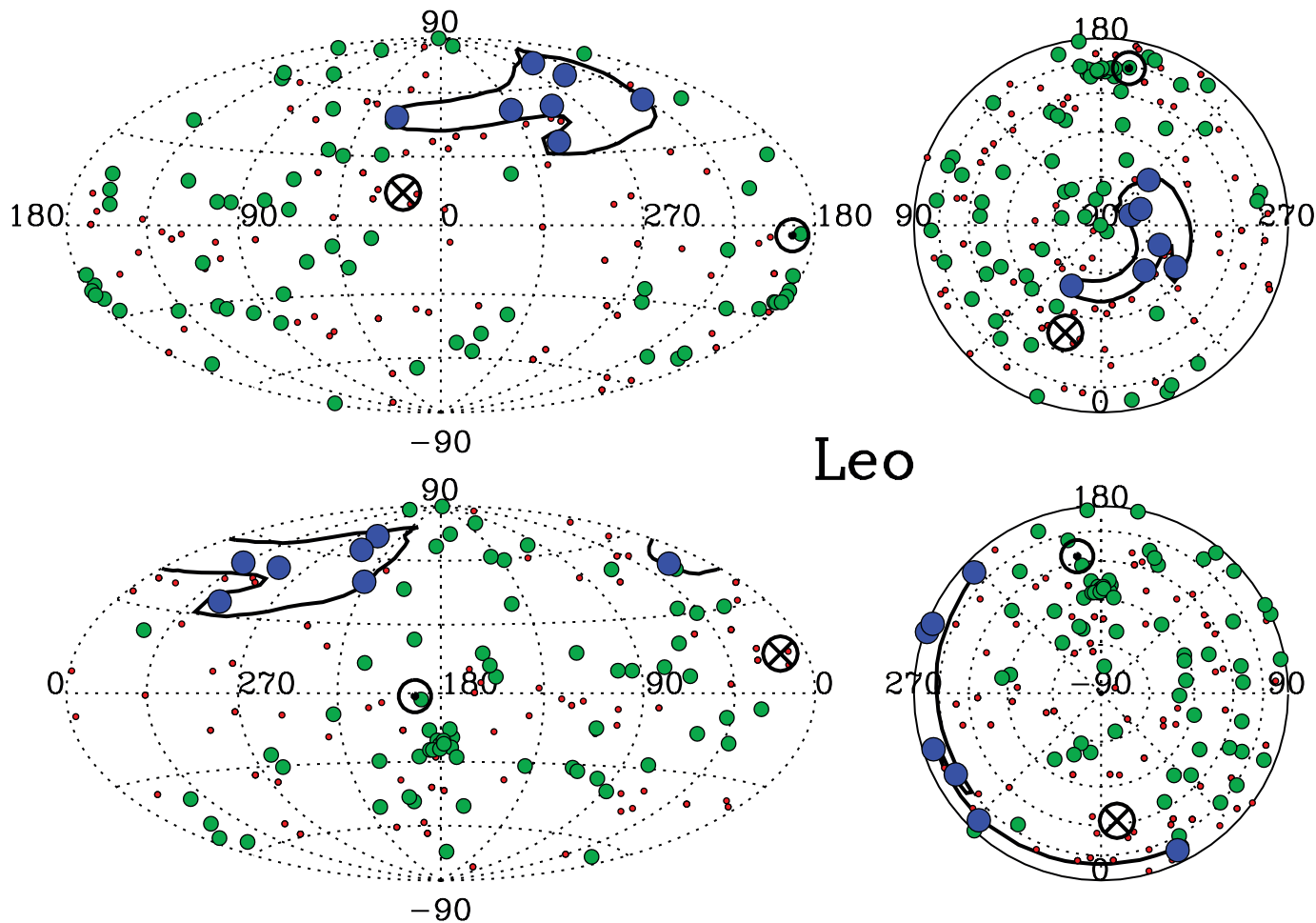
FIG. 12.—Same as Fig. 1, but for the Leo Cloud.

explanations for the observed correlation. Dust destruction in the warm partially ionized ISM is often discussed in the context of shocks produced by supernovae (Savage & Sembach 1996; Jones et al. 1994). Shocks may also be produced in the LISM from either turbulent motions possibly driven by shear flow interactions between clouds or direct macroscopic collisions of clouds. The thermal sound speed $c_s = (nkT/\rho)^{1/2}$, using LISM densities from Redfield (2006) and the mean LISM temperature from Redfield & Linsky (2004b), is ∼8 km s^{-1}. For the clouds with the highest turbulence (e.g., Mic and Eri), the sight-line–averaged turbulent velocity is ∼3.5 km s^{-1}, which results in a turbulent Mach number (M_ξ) of ∼0.4. Although there may be regions of enhanced turbulent motions, perhaps at the interaction boundaries of clouds, average turbulent velocities are not high enough to produce shocks.

Macroscopic velocity differences between the 15 LISM clouds can be significantly greater than the sound speed if they are interacting. Figure 22 shows the distribution of predicted velocity differences (ΔV) between the 15 LISM clouds when multiple clouds are predicted to lie along a line of sight. For a uniform sample of hypothetical individual sight lines across the entire sky, we use the boundaries shown in Figures 1–15 to determine how many of the 15 LISM clouds are expected to lie along each of the hypothetical lines of sight. If multiple clouds are predicted to lie along the line of sight, we calculate all possible cloud velocity differences, which are shown in Figure 22. For example, a hypothetical sight line that traverses two clouds (e.g., at $l = 270°$

and $b = 0°$ where the G and Cet Clouds overlap) will provide one velocity difference measurement in Figure 22, whereas if three clouds are predicted along the line of sight (e.g., at $l = 165°$ and $b = 0°$ where the LIC, Aur, and Hyades Clouds overlap), three possible velocity difference measurements are shown. Calculating the radial and transverse components of a velocity vector of LISM material along an arbitrary line of sight requires projecting the velocity vector (V_0, l_0, b_0) along the radial and transverse unit vectors in the arbitrary direction (l, b). The magnitudes of the radial and transverse velocities are calculated from

$$V_r = V_0[\cos b \cos b_0 \cos(l_0 - l) + \sin b_0 \sin b], \quad (1)$$
$$V_l = V_0 \cos b_0 \sin(l_0 - l), \quad (2)$$
$$V_b = V_0[\sin b_0 \cos b - \cos b_0 \sin b \cos(l_0 - l)]. \quad (3)$$

Since we do not have a fully three-dimensional model of these LISM clouds (i.e., we do not know which clouds are in fact adjacent and actively interacting), we do not know whether all these velocity differences are actually realized. However, a large percentage of the possible velocity differences are supersonic and thus could cause shocks where adjacent clouds meet.

The question of grain destruction/erosion involves many factors, including grain size, composition, porosity, the relative speed of collisions with other grains or particles, compression ratio in shocks, grain charge, magnetic fields, and turbulence. This topic has been addressed by a number of authors (e.g., Jones et al.
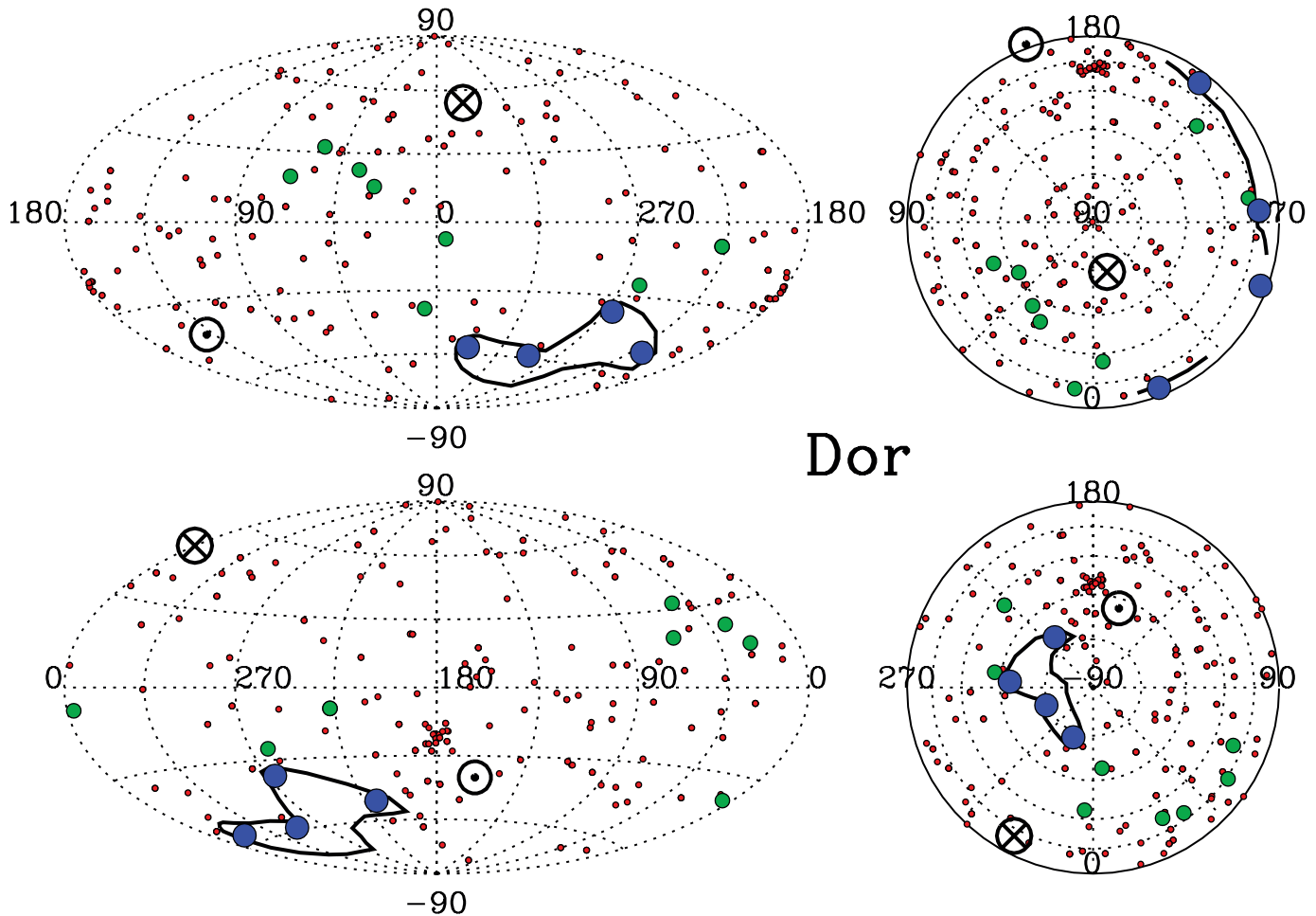
FIG. 13.—Same as Fig. 1, but for the Dor Cloud.

1996). Frisch et al. (1999) and others showed that the observed Fe and Mg ions in warm gas like the LIC come from grain destruction whether by shocks, grain-grain collisions, or other physical processes. Since most of the Fe and Mg in the LIC are locked up in grains, small differences in grain destruction between or within clouds can produce large differences in the gas-phase abundances of these elements. High-speed supernova-generated shocks (50–200 km s^{-1}) are often cited as the main grain destruction method, but grain-grain collisions with relative velocities exceeding only 2.7 km s^{-1} for silicate grains or 1.2 km s^{-1} for carbonaceous grains can lead to grain shattering (Jones et al. 1996). Velocities exceeding these values are typically found between two clouds along the same line of sight (Fig. 22) and are similar to the measured cloud turbulent velocities. Given that interstellar dust grains are typically charged and the ISM is magnetized and turbulent, Yan et al. (2004) showed that MHD turbulence can accelerate the grains through gyroresonance interactions leading to supersonic grain speeds, grain-grain collisions, and shattering. This process could be the physical basis for the observed correlation of low metal depletions with high turbulent velocities.

5.3. Connection with Radio Scintillation Screens

For many years, radio observers have called attention to a rapid variability of certain quasars and pulsars on hourly to yearly timescales that has been attributed to interstellar scintillation. The scattering screens responsible for the scintillation are generally assumed to be turbulent regions of enhanced electron density.

Extensive monitoring of a source and measurement of time delays as seen by widely separated radio telescopes provide critical data for estimating the distance to the scattering screen, as well as its size, transverse velocity, and shape. In their VLA[7] survey of northern sky active galactic nuclei for rapid intraday variability, Lovell et al. (2007) found that 56% of the sources are variable on timescales of hours to several days, but rapid variability indicative of nearby scattering screens is rare, indicating that nearby scattering screens cover only a small fraction of the sky.

Studies of intraday variability of three quasars (J1819+3845, PKS 1257−326, and PKS 0405−385) and two pulsars (PSR J0437−4715 and PSR B1133+16) find that some scattering screens lie within the LISM at short distances from the Sun, although the distances have significant uncertainty and are model dependent. For example, Dennett-Thorpe & de Bruyn (2003) and Macquart & de Bruyn (2006) estimate that the scattering screen toward J1819+3845 is only 1−12 pc from the Sun. Bignall et al. (2006) found that the scattering screen toward PKS 1257−3826 lies at a distance somewhat closer than 10 pc. Rickett et al. (2002) place the anisotropic scattering screen toward PKS 0405−385 at between 2 and 30 pc from the Sun with a preferred distance of 25 pc, although analysis of more recent data by Kedziora-Chudczer (2006) suggests a distance of about 10 pc. Smirnova et al. (2006) show
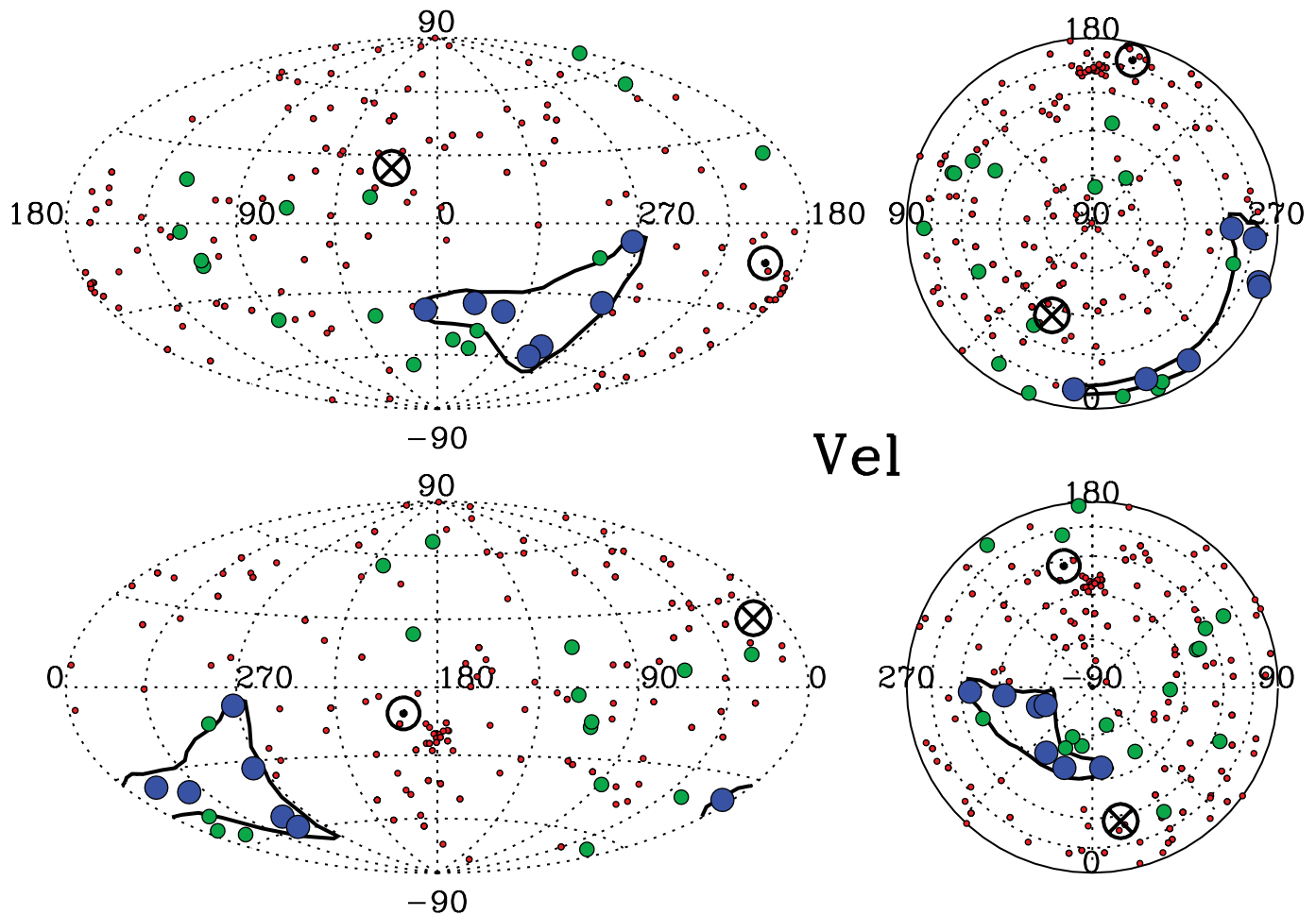
FIG. 14.—Same as Fig. 1, but for the Vel Cloud.

that the scattering screen toward PSR J0437−4715 also lies at about 10 pc from the Sun and is likely the same screen that causes the scintillation of PKS 0405−385, which is only 10° away. If so, this scattering screen is extended rather than very restricted in size. Putney & Stinebring (2006) present six pulsars that show evidence of multiple scintillation screens along their line of sight, the vast majority of which are located well beyond the LB. One of their nearest pulsars, PSR B1133+16, shows evidence for a nearby scintillation screen only 21.6 pc from the Sun. Several other scintillating quasars, or intraday variables, show annual cycles that may provide constraints on the distance to the scintillation screen, such as B0917+624 (Rickett et al. 2001; Jauncey & Macquart 2001) and PKS 1519−273 (Jauncey et al. 2003).

We find that the five nearby scattering screens all lie close to the edges of several of our dynamical clouds, as indicated in Figure 19, where the direction of the radio scintillation sources is indicated by stars. In particular, three of the five lie near the interface of the LIC and G Cloud. The radial velocity differences between the LIC and G Cloud in these directions are generally quite small (i.e., $\sim$1 km s^{-1}). However, the transverse motion differences between the LIC and G Cloud in these directions can be quite substantial, reaching 6–7 km s^{-1}. These regions of significant transverse velocity differences could induce shear flows and generate turbulence. The annual variation of the scintillation timescale of intraday variables is a function of the diffraction pattern of the screen and its transverse velocity. With our rigid velocity vectors of LISM clouds, we are able to calculate the transverse motions of local clouds. Even with just a handful of

sight lines, we can investigate the relationship between the LISM and the scintillation screens, but many more radio scintillation and high-resolution LISM absorption line observations are needed, together with a fully three-dimensional morphological and kinematic model of the warm LISM, in order to fully explore the physical connection between warm clouds and scintillation screens. Linsky et al. (2008) more fully explore the relationship between scattering screens and LISM clouds, including a direct comparison of the transverse velocities of the screens and the clouds.

5.4. Connection with Cold Dense Structures in the LISM

In their 21 cm absorption line study of the warm and cold neutral interstellar gas, Heiles & Troland (2003) mapped a region of cold gas centered at $l = 225°$, $b = 44°$ that extends over 30° in Galactic longitude. They found that the gas temperature is about 25 K. Meyer et al. (2006) observed narrow Na I absorption due to this cold cloud toward a series of nearby stars and confirm a cloud temperature $\sim$20 K and turbulent velocity of $\sim$0.4 km s^{-1}. Based on the well-known distances of the observed stars, they were able to show that the distance to this cold gas must be less than 41 pc, with a corresponding aspect ratio (length perpendicular to the line of sight vs. length along the line of sight) of 70 : 1. However, the cloud could be as close as 2 pc. Thus, the cold gas structure is located inside the LISM.

The Galactic coordinates of the cold gas correspond to a region that is not clearly a part of any individual warm cloud (see Fig. 19), but near the boundaries of several clouds, including the LIC, G, Aur, Gem, and Leo Clouds. In particular, the Gem Cloud
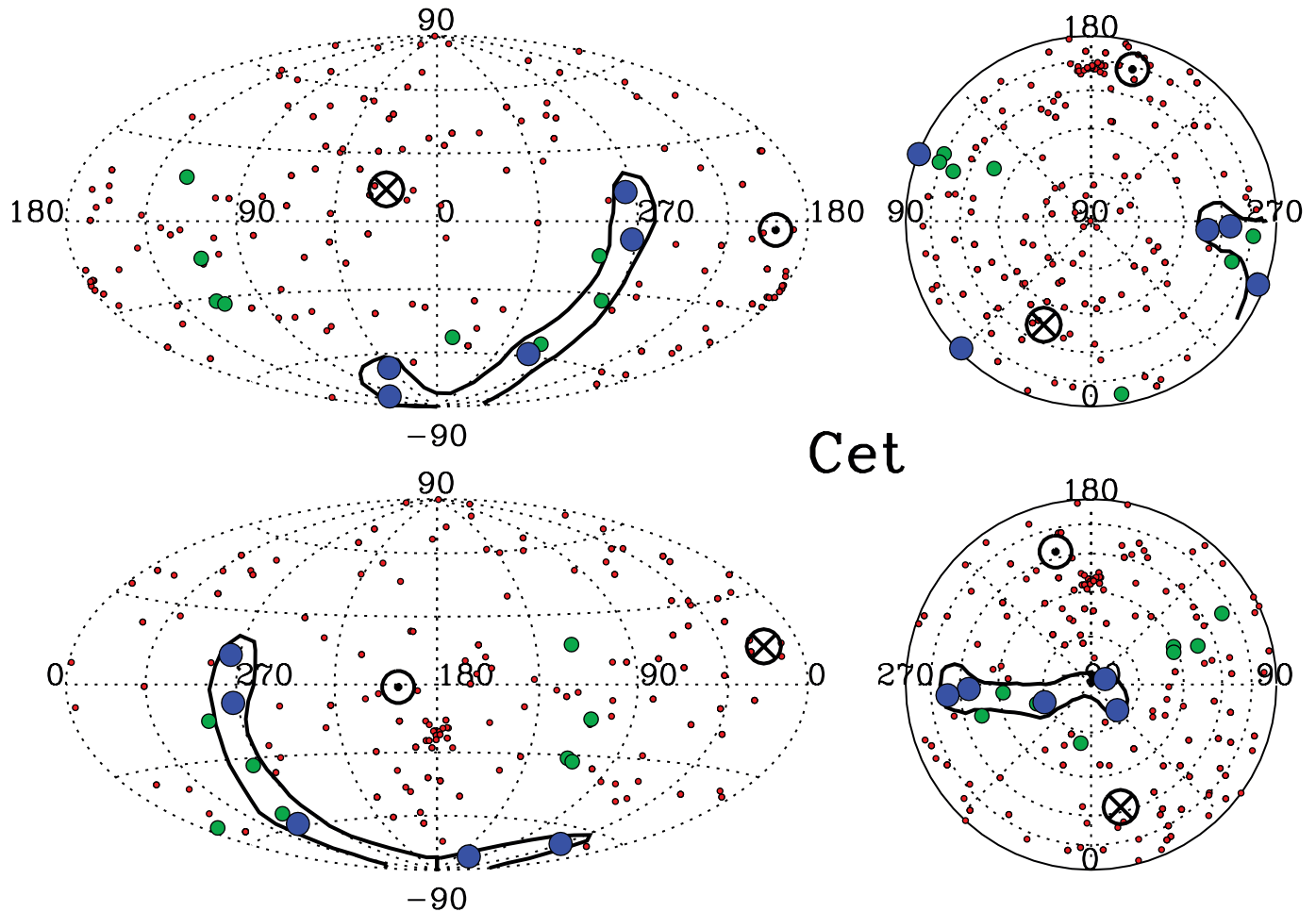
Fig. 15.—Same as Fig. 1, but for the Cet Cloud. Note that the boundaries of the Cet Cloud include a couple sight lines that were not used in the velocity vector calculation, which nonetheless have consistent projected velocities (i.e., green circle sight lines) and therefore may traverse Cet Cloud material.

has a high radial velocity in the direction of the cold cloud, ~24 km s^{-1}, whereas the other clouds have modest radial velocities, ranging from 8 to 12 km s^{-1}. The resulting high radial velocity differences are indicated in Figure 22. Along this line of sight, the high radial velocity (~24 km s^{-1}) Gem Cloud may be compressing material as it collides with slow moving Leo and Aur (~12 km s^{-1}), and ultimately the LIC (~10 km s^{-1}). The heliocentric velocity (~11.5 km s^{-1}) of the cold material observed by Meyer et al. (2006) matches well with the velocity of the slow moving Leo and Aur Clouds, as expected if it was formed by the compression of the Gem Cloud against the Leo and Aur Clouds, and the cold material may actually be physically associated with the warm material observed in the Leo and Aur Clouds.

The collision of warm gas clouds to produce small sheetlike cold neutral clouds has been explored through detailed simulations of a turbulent ISM (e.g., Vázquez-Semadeni et al. 2006; Audit & Hennebelle 2005). Also McKee & Ostriker (1977) predicted that cold neutral clouds must be surrounded by warm clouds (in pressure equilibrium in their model) to shield the cold gas from UV and X-ray heating and ionization. Our rigid velocity vector solutions certainly indicate that in the direction of the cold cloud, relatively large kinematic differences exist between clouds (e.g., the Gem Cloud is moving ~12 km s^{-1} faster than the Leo and Aur Clouds and ~14 km s^{-1} faster than the LIC and G Cloud). Given that the farthest distance limit for the five clouds in the proximity of the cold cloud line of sight is 11.1 pc (the Leo Cloud) and that the limit on the Gem Cloud is 6.7 pc, these five clouds are in very

close proximity in distance as well, and collisions between these warm clouds are likely. In particular, it is critical to have a collision of material along the radial direction to maximize the chances of detection. Because of the extreme aspect ratio of this cloud, if it were oriented along the line of sight, the projection on the sky would be extremely small. Further work on the distances of both the warm LISM clouds and the cold cloud is needed to determine whether there is a spatial and dynamical connection between these interstellar structures.

5.5. The Transition between the LIC and G Cloud

Until now, we have assumed that individual clouds are rigid structures, each with a simple velocity vector characterizing all of the included sight lines within the radial velocity measurement errors. This simple approximation may not be valid, as shown by two sets of data. One, noted in § 2.3, is that the velocity and, to a lesser degree of significance, the temperature of interstellar gas flowing through the heliosphere are intermediate in value between the corresponding quantities in the LIC and G Cloud (see Table 16), implying that the heliosphere lies in a transition zone between the two clouds where there is a gradient in properties. The other evidence is that Redfield & Linsky (2001) noted that the components assigned to the LIC in the direction of the Hyades have radial velocities 2.9 km s^{-1} smaller than predicted by the Lallement & Bertin (1992) LIC vector. These smaller radial velocities suggest a deceleration of the LIC flow in the forward direction, where it may be interacting with the Hyades Cloud. We

TABLE 1
LIC Sᴵɢʜᴛ-Lᴵɴᴇ Pʀᴏᴘᴇʀᴛᴵᴇs

Star Name	HD	d (pc)	v (km s^{-1})	σ^{a}	log N(H I) (cm^{-2})	T (K)	ξ (km s^{-1})	D(Fe)	D(Mg)	Other Clouds[b]
α CMa A	48915	2.6	18.55	0.12	17.2	8000^{+500}_{-1000}	0.5 ± 0.3	$-0.75^{+0.15}_{-0.21}$	$-0.54^{+0.17}_{-0.22}$	...
α CMa B.................	48915B	2.6	17.60	0.51	17.6	8000^{+500}_{-1000}	0.5 ± 0.3	...	...	...
ϵ Eri........................	22049	3.2	18.73	0.70	17.8	7410^{+860}_{-830}	$2.03^{+0.41}_{-0.45}$	-1.03 ± 0.17	-0.81 ± 0.12	...
α CMi	61421	3.5	19.76	0.78	17.9	6710^{+660}_{-630}	$1.21^{+0.35}_{-0.45}$	-1.13 ± 0.07	-1.31 ± 0.10	Aur
ϵ Ind	209100	3.6	-9.20	0.02	18.0	<9850	...	...	...	Vel
τ Cet........................	10700	3.6	12.34	0.20	18.0	<6700	...	...	...	G, Blue
40 Eri A	26965	5.0	21.73	0.58	17.8	8120 ± 450	$0.5^{+1.2}_{-0.5}$	...	-0.90 ± 0.10	...
η Cas A	4614	6.0	11.18	0.67	...	...	...	...	...	...
α PsA	216956	7.7	-5.87	0.42	...	...	...	...	...	Mic
α Lyr	172167	7.8	-12.90	0.30	...	...	...	...	...	G
χ^1 Ori	39587	8.7	23.08	0.38	17.8	7000^{+730}_{-680}	$2.38^{+0.15}_{-0.17}$	-1.03 ± 0.07	-0.74 ± 0.09	...
δ Eri........................	23249	9.0	19.60	0.07	17.9	<8900	...	...	...	Blue, Hyades
κ^1 Cet......................	20630	9.2	20.84	0.31	17.5	5200^{+1900}_{-1700}	$2.64^{+0.28}_{-0.32}$	-1.01 ± 0.17	-0.68 ± 0.16	...
CF UMa	103095	9.2	2.05	1.19	...	...	...	...	...	...
β Gem	62509	10.3	19.65	0.60	18.0	9000^{+1600}_{-1500}	$1.67^{+0.27}_{-0.32}$	-1.23 ± 0.12	-1.01 ± 0.14	...
EP Eri	17925	10.4	19.50	0.88	18.0	8100 ± 1300	2.46 ± 1.45	...	-0.48 ± 0.42	G, Blue
γ Ser........................	142806	11.1	-18.19	0.93	...	...	...	...	...	Mic, Leo
13 Per	16895	11.2	16.45	0.46	...	...	...	...	...	...
HR 1925	37394	12.2	17.50	1.25	18.3	<9900	...	...	...	Aur
α Aur	34029	12.9	21.48	0.82	18.2	6700^{+1400}_{-1300}	$1.68^{+0.32}_{-0.39}$	-1.21 ± 0.06	-0.95 ± 0.10	...
HR 8	166	13.7	6.50	0.44	18.3	<10700	...	...	...	Eri, Hyades
α Oph........................	159561	14.3	-22.57	1.68	...	...	...	...	...	...
72 Her	157214	14.4	-15.51	0.33	...	...	...	...	...	...
α Cep	203280	15.0	0.20	0.54	...	...	...	...	...	...
σ Boo	128167	15.5	-2.58	0.63	...	...	...	...	...	...
99 Her	165908	15.7	-17.43	1.54	...	...	...	...	...	G
β Cas........................	432	16.7	9.15	0.69	18.2	9760^{+800}_{-880}	$0.0^{+1.1}_{-0.0}$	-1.28 ± 0.16	-1.28 ± 0.17	...
DX Leo	82443	17.7	11.00	0.22	17.7	8540 ± 850	1.78 ± 1.77	...	-0.83 ± 0.20	...
τ^6 Eri	23754	17.9	16.99	0.04	...	...	...	...	...	...
V368 Cep.................	220140	19.7	6.00	0.19	18.0	12050^{+820}_{-790}	$0.0^{+1.0}_{-0.0}$	...	-0.78 ± 0.17	...
α Tri	11443	19.7	17.89	1.84	18.1	7700^{+3100}_{-2600}	$0.0^{+1.7}_{-0.0}$	-1.16 ± 0.23	-1.44 ± 0.15	...
HR 4345...................	97334	21.7	4.30	0.14	17.8	<8700	...	...	...	NGP
PW And	1405	21.9	8.50	0.13	18.1	11300^{+1900}_{-1800}	$0.0^{+1.6}_{-0.0}$	...	-0.48 ± 0.52	Eri, Hyades
SAO 136111	73350	23.6	12.00	0.50	18.2	<11400	...	...	...	G, Aur
δ UMa	106591	25.0	3.80	1.65	...	...	...	...	...	...
β Aur........................	40183	25.2	22.30	1.74	...	...	...	...	...	...
γ UMa......................	103287	25.6	4.40	1.54	...	...	...	...	...	...
λ And	222107	25.8	6.50	0.03	18.5	<13100	...	...	...	Hyades
σ Cet	15798	25.8	15.99	0.81	...	...	...	...	...	...
τ^3 Eri	18978	26.4	15.90	0.82	...	...	...	...	...	...
HR 860.....................	17948	26.5	15.10	0.31	...	...	...	...	...	...
SAO 32862	198084	27.1	-2.60	0.71	...	...	...	...	...	...
HR 1099...................	22468	29.0	21.90	0.88	17.9	7900 ± 1500	1.18 ± 0.47	<-1.12	-1.28 ± 0.10	...
θ Peg	210418	29.6	-4.20	1.30	...	...	...	...	...	Eri
SAO 85045	157466	29.8	-19.02	0.96	...	...	...	...	...	...
η Ari........................	13555	30.1	16.99	0.50	...	...	...	...	...	Hyades
δ Cas	8538	30.5	13.05	1.06	...	...	...	...	...	...
α Gru	209952	31.1	-10.93	0.58	...	...	...	...	...	Vel
α Lac........................	213558	31.4	3.50	1.11	...	...	...	...	...	Hyades
DK UMa	82210	32.4	9.41	0.06	17.9	6750 ± 240	$1.35^{+0.18}_{-0.20}$	-1.10 ± 0.07	-0.87 ± 0.09	...
ϵ Gru	215789	39.7	-7.30	0.43	...	...	...	...	...	Vel
SAO 76593	27808	40.9	23.10	0.17	...	...	...	...	...	Aur
SAO 93981	28568	41.2	23.90	0.39	18.0	<11700	...	...	-0.97 ± 0.18	Aur
SAO 111879	28736	43.2	21.60	1.51	...	...	...	...	...	Aur
101 Tau	31845	43.3	22.40	1.44	...	...	...	...	...	Aur
SAO 94033	29225	43.5	22.50	1.10	...	...	...	...	...	Aur
SAO 93982	28608	43.6	23.20	0.20	...	...	...	...	...	Aur
SAO 76683	29419	44.2	23.20	0.25	...	...	...	...	...	Aur
V993 Tau	28205	45.8	23.30	0.14	18.0	<11200	...	...	-0.94 ± 0.29	Aur
SAO 93963	28406	46.3	22.10	1.37	...	...	...	...	...	Aur
SAO 76609	28033	46.4	23.60	0.28	18.2	<12900	...	...	-0.79 ± 0.36	Aur
V471 Tau	...	46.8	20.90	0.52	18.2	<11000	...	...	...	Aur, Hyades
SAO 93945	28237	47.2	22.40	0.98	...	...	...	...	...	Aur
SAO 93831	26784	47.4	23.00	0.05	...	...	...	...	...	Aur

TABLE 1 — *Continued*

Star Name	HD	d (pc)	v (km s^{-1})	σ[a]	log N(H I) (cm^{-2})	T (K)	ξ (km s^{-1})	D(Fe)	D(Mg)	Other Clouds[b]
γ Aqr	212061	48.4	−4.52	0.76	...	...	...	...	...	...
SAO 56530	21847	48.9	21.10	0.39	...	...	...	...	...	...
SAO 93885	27561	51.4	22.20	1.11	...	...	...	...	...	Aur
κ And	222439	52.0	7.60	1.06	...	...	...	...	...	Hyades
δ Cyg	186882	52.4	−9.60	1.47	...	...	...	...	...	G
SAO 93913	27848	53.4	22.40	0.98	...	...	...	...	...	Aur
HR 1608	32008	54.7	21.60	0.07	17.8	...	...	...	...	Blue
45 Aur	43905	57.0	18.47	0.13	...	...	...	...	...	...
ζ Peg	214923	64.1	−2.20	0.34	...	...	...	...	...	Eri
ι Cap	203387	66.1	−12.06	0.06	17.9	12900^{+3800}_{-3300}	$1.58^{+0.56}_{-0.89}$	-0.85 ± 0.36	-0.22 ± 0.43	...
η Aur	32630	67.2	23.00	0.94	...	...	...	...	...	...
G191-B2B	...	68.8	19.19	0.09	18.2	6200^{+1400}_{-1300}	$1.78^{+0.40}_{-0.51}$	-1.18 ± 0.09	-0.97 ± 0.10	...
ι Oph	152614	71.7	−21.50	0.13	...	...	...	...	...	...
Feige 24	...	74.4	17.60	0.17	18.1	...	...	...	...	Hyades
γ Ori	35468	74.5	25.40	1.88	...	...	...	...	...	Aur

[a] Parameter $\sigma = (|v_0 - v_\star|)/\sigma_v$, where we have imposed a minimum σ_v of 1 km s^{-1} for all high-resolution data and a minimum σ_v of 3 km s^{-1} for all medium-resolution data.

[b] Other dynamical clouds for which the observed velocity is within 3 σ of the predicted value and the sight line is closer than 10° to the cloud. These are less likely but possible dynamical assignments for these sight lines.

now find that these absorption components have radial velocities $\sim$1.0 km s^{-1} smaller than predicted by the new LIC vector. As a test, we removed these 16 components from the LIC vector calculation and found that the vector velocity amplitude increased by only 0.39 km s^{-1}. This does not change our conclusion that the heliosphere is in a transition zone between the LIC and G Cloud, or that the LIC is decelerated at its forward edge.

We also considered whether the LIC and G Cloud are really one cloud with a gradient of physical properties across their combined length. We tested this hypothesis by plotting the physical parameters for the LIC and G Cloud sight lines with respect to angle relative to the downwind direction (Fig. 23) and with respect to the hydrogen column density (Fig. 24). No correlation exists between angle and hydrogen column density. Since the LIC is mostly in the downwind direction and the G Cloud mostly in the upwind direction, the angle from the downwind direction is a discriminant between the two clouds. With only one exception, the gas temperatures for LIC sight lines are all larger than for the G Cloud sight lines, implying that the two-cloud approximation is valid. We note, however, a trend of higher LIC temperatures with

TABLE 2
G CLOUD SIGHT-LINE PROPERTIES

Star Name	HD	d (pc)	v (km s^{-1})	σ[a]	log N(H I) (cm^{-2})	T (K)	ξ (km s^{-1})	D(Fe)	D(Mg)	Other Clouds[b]
α Cen B	128621	1.3	−18.14	0.02	17.6	5500^{+330}_{-320}	$1.37^{+0.34}_{-0.41}$	-0.53 ± 0.14	-0.38 ± 0.14	...
α Cen A	128620	1.3	−18.45	0.33	17.6	5100^{+1200}_{-1100}	$1.21^{+0.33}_{-0.49}$	-0.61 ± 0.06	-0.42 ± 0.11	...
70 Oph	165341	5.1	−26.50	0.07	17.8	2700^{+3000}_{-2300}	$3.64^{+0.42}_{-0.44}$	-0.38 ± 0.09	0.22 ± 0.20	Mic
36 Oph A	155886	5.5	−28.40	0.17	17.8	5870 ± 560	$2.33^{+0.46}_{-0.51}$	-0.61 ± 0.26	-0.29 ± 0.18	...
α Lyr	172167	7.8	−16.86	1.33	...	...	...	...	...	Mic
AB Dor	36705	14.9	5.19	0.15	...	...	...	...	...	Blue, Dor
LQ Hya	82558	18.3	6.50	0.23	18.8	5700^{+6300}_{-5700}	2.52 ± 1.26	...	-1.38 ± 0.31	LIC, Aur
α Hyi	12311	21.9	4.90	0.76	...	...	...	...	...	Cet
δ Vel	74956	24.4	1.30	1.18	...	...	...	...	...	...
ζ Aql	177724	25.5	−21.30	0.30	...	...	...	...	...	Eri
σ Cet	15798	25.8	21.85	0.39	...	...	...	...	...	...
τ^3 Eri	18978	26.4	20.90	0.12	...	...	...	...	...	...
HR 4023	88955	31.5	−1.70	0.36	...	...	...	...	...	...
SAO 68491	184499	32.0	−14.28	0.41	...	...	...	...	...	LIC
β Car	80007	34.1	−4.32	1.55	...	...	...	...	...	...
μ Vel	93497	35.3	−4.38	0.41	18.5	<10500	...	...	...	Cet
β Lib	135742	49.1	−26.90	0.61	...	...	...	...	...	...
o Ser	160613	51.5	−29.00	0.33	...	...	...	...	...	Oph
SAO 159459	140283	57.3	−28.55	0.02	...	...	...	...	...	Gem
ν Ser	156928	59.3	−27.70	1.49	...	...	...	...	...	Mic
HD 141569	141569	99.0	−28.70	0.22	...	...	...	...	...	Gem

[a] Parameter $\sigma = (|v_0 - v_\star|)/\sigma_v$, where we have imposed a minimum σ_v of 1 km s^{-1} for all high-resolution data and a minimum σ_v of 3 km s^{-1} for all medium-resolution data.

[b] Other dynamical clouds for which the observed velocity is within 3 σ of the predicted value and the sight line is closer than 10° to the cloud. These are less likely but possible dynamical assignments for these sight lines.

TABLE 3
Blue Cloud Sight-Line Properties

Star Name	HD	d (pc)	v (km s^{-1})	σ^{a}	log N(H I) (cm^{-2})	T (K)	ξ (km s^{-1})	D(Fe)	D(Mg)	Other Clouds[b]
α CMa A	48915	2.6	12.70	0.04	17.2	3000^{+2000}_{-1000}	2.7 ± 0.3	$-0.95^{+0.15}_{-0.21}$	$-0.77^{+0.17}_{-0.22}$	...
α CMa B	48915B	2.6	11.70	0.63	...	3000^{+2000}_{-1000}	2.7 ± 0.3	...	...	...
EP Eri	17925	10.4	9.00	0.65	...	...	...	...	...	LIC
ζ Dor	33262	11.7	8.41	0.25	17.8	7700^{+2300}_{-2100}	$2.34^{+0.38}_{-0.48}$	-0.52 ± 0.30	-0.05 ± 0.27	G
HR 2225	43162	16.7	14.00	0.44	17.9	<10400	...	...	...	LIC
β Pic	39060	19.3	10.12	0.81	...	...	...	...	...	...
HR 2882	59967	21.8	8.40	0.47	18.5	<15100	...	...	...	...
σ Cet	15798	25.8	9.74	0.38	...	...	...	...	...	...
β Car	80007	34.1	3.57	0.24	...	...	...	...	...	Vel, Cet
α Car	45348	95.9	8.19	0.58	...	...	...	...	...	Dor

[a] Parameter $\sigma = (|v_0 - v_\star|)/\sigma_v$, where we have imposed a minimum σ_v of 1 km s^{-1} for all high-resolution data and a minimum σ_v of 3 km s^{-1} for all medium-resolution data.
[b] Other dynamical clouds for which the observed velocity is within 3 σ of the predicted value and the sight line is closer than 10° to the cloud. These are less likely but possible dynamical assignments for these sight lines.

TABLE 4
Aql Cloud Sight-Line Properties

Star Name	HD	d (pc)	v (km s^{-1})	σ^{a}	log N(H I) (cm^{-2})	T (K)	ξ (km s^{-1})	D(Fe)	D(Mg)	Other Clouds[b]
61 Cyg A	201091	3.5	-3.00	1.28	17.8	6850 ± 880	2.08 ± 0.64	...	-0.95 ± 0.22	LIC
α Aql	187642	5.1	-20.90	0.14	17.9	12600 ± 2400	$0.63^{+0.90}_{-0.63}$	-0.96 ± 0.54	-0.69 ± 0.55	G, Eri
70 Oph	165341	5.1	-43.34	0.92	17.1	3300 ± 2100	2.31 ± 0.37	...	-0.57 ± 0.15	...
HR 6748	165185	17.4	-29.20	0.36	18.1	<15700	...	...	...	G
ζ Aql	177724	25.5	-30.20	0.79	...	...	...	...	...	Oph
λ Aql	177756	38.4	-30.70	1.19	...	...	...	...	...	Mic
BO Mic	197890	44.4	0.00	0.31	...	...	...	...	...	...
δ Cyg	186882	52.4	-18.80	0.71	...	...	...	...	...	Mic
α Del	196867	73.8	-10.40	1.01	...	...	...	...	...	...

[a] Parameter $\sigma = (|v_0 - v_\star|)/\sigma_v$, where we have imposed a minimum σ_v of 1 km s^{-1} for all high-resolution data and a minimum σ_v of 3 km s^{-1} for all medium-resolution data.
[b] Other dynamical clouds for which the observed velocity is within 3 σ of the predicted value and the sight line is closer than 10° to the cloud. These are less likely but possible dynamical assignments for these sight lines.

TABLE 5
Eri Cloud Sight-Line Properties

Star Name	HD	d (pc)	v (km s^{-1})	σ^{a}	log N(H I) (cm^{-2})	T (K)	ξ (km s^{-1})	D(Fe)	D(Mg)	Other Clouds[b]
61 Cyg A	201091	3.5	-9.00	0.27	17.8	6850 ± 880	2.08 ± 0.64	...	-0.35 ± 0.22	...
α Aql	187642	5.1	-17.10	1.04	17.9	12300^{+2000}_{-2200}	$0.0^{+1.2}_{-0.0}$	-0.86 ± 0.27	-0.67 ± 0.28	G
λ Aql	177756	38.4	-21.90	0.35	...	...	...	...	...	G
α Peg	218045	42.8	-0.90	0.12	...	...	...	...	...	LIC
V376 Peg	209458	47.1	-6.60	0.00	18.4	<15900	...	...	...	...
υ Peg	220657	53.1	1.73	0.13	17.9	1700^{+1100}_{-900}	3.93 ± 0.22	-0.35 ± 0.08	0.01 ± 0.12	LIC
α Del	196867	73.8	-14.00	0.14	...	...	...	...	...	...
θ Aql	191692	88.0	-17.70	0.15	...	...	...	...	...	Aql

[a] Parameter $\sigma = (|v_0 - v_\star|)/\sigma_v$, where we have imposed a minimum σ_v of 1 km s^{-1} for all high-resolution data and a minimum σ_v of 3 km s^{-1} for all medium-resolution data.
[b] Other dynamical clouds for which the observed velocity is within 3 σ of the predicted value and the sight line is closer than 10° to the cloud. These are less likely but possible dynamical assignments for these sight lines.

TABLE 6
Aur Cloud Sight-Line Properties

Star Name	HD	d (pc)	v (km s^{-1})	σ[a]	log N(H I) (cm^{-2})	T (K)	ξ (km s^{-1})	D(Fe)	D(Mg)	Other Clouds[b]
α CMi	61421	3.5	23.00	1.03	17.6	6710^{+660}_{-630}	$1.21^{+0.35}_{-0.45}$	-1.13 ± 0.07	-0.79 ± 0.10	. . .
LQ Hya	82558	18.3	14.00	0.19	. . .	. . .	. . .	. . .	. . .	LIC, G
α Tau......................	29139	20.0	20.62	1.29	17.8	. . .	. . .	. . .	. . .	LIC
SAO 93801	26345	43.1	21.10	0.51	. . .	. . .	. . .	. . .	. . .	LIC
SAO 93973	28483	50.2	20.80	0.31	. . .	. . .	. . .	. . .	. . .	LIC
γ Crv	106625	50.6	-2.00	0.32	. . .	. . .	. . .	. . .	. . .	. . .
45 Aur	43905	57.0	11.87	0.60	. . .	. . .	. . .	. . .	. . .	. . .
η Aur.......................	32630	67.2	17.44	0.87	. . .	. . .	. . .	. . .	. . .	. . .
HR 2324.................	45320	70.1	26.00	1.18	. . .	. . .	. . .	. . .	. . .	. . .

[a] Parameter $\sigma = (|v_0 - v_\star|)/\sigma_v$, where we have imposed a minimum σ_v of 1 km s^{-1} for all high-resolution data and a minimum σ_v of 3 km s^{-1} for all medium-resolution data.

[b] Other dynamical clouds for which the observed velocity is within 3 σ of the predicted value and the sight line is closer than 10° to the cloud. These are less likely but possible dynamical assignments for these sight lines.

TABLE 7
Hyades Cloud Sight-Line Properties

Star Name	HD	d (pc)	v (km s^{-1})	σ[a]	log N(H I) (cm^{-2})	T (K)	ξ (km s^{-1})	D(Fe)	D(Mg)	Other Clouds[b]
EV Lac......................	. . .	5.0	7.30	0.12	18.0	<8300	. . .	. . .	. . .	LIC, Eri
κ^1 Cet......................	20630	9.2	13.35	1.11	17.5	3600^{+2900}_{-2200}	$2.17^{+0.34}_{-0.52}$	-1.29 ± 0.25	-0.79 ± 0.19	. . .
α Tri............................	11443	19.7	13.65	0.16	17.8	8900^{+3900}_{-3400}	$1.3^{+1.7}_{-1.3}$	-0.97 ± 0.23	-0.58 ± 0.15	LIC
HR 1099..................	22468	29.0	14.80	0.63	17.6	8800^{+800}_{-1100}	$0.0^{+0.9}_{-0.0}$	<-0.82	$-1.36 \pm 0.0.09$	. . .
SAO 93801	26345	43.1	13.60	0.08	. . .	. . .	. . .	. . .	. . .	. . .
SAO 111879	28736	43.2	13.40	0.19	. . .	. . .	. . .	. . .	. . .	. . .
SAO 76683	29419	44.2	12.30	0.54	. . .	. . .	. . .	. . .	. . .	. . .
V993 Tau	28205	45.8	14.80	0.84	. . .	. . .	. . .	. . .	. . .	. . .
SAO 93831	26784	47.4	15.50	1.62	. . .	. . .	. . .	. . .	. . .	. . .
SAO 93885	27561	51.4	14.40	0.86	. . .	. . .	. . .	. . .	. . .	. . .
υ Peg................................	220657	53.1	8.80	0.51	17.4	1000^{+1900}_{-1000}	$3.4^{+0.61}_{-0.63}$	-0.87 ± 0.45	-1.07 ± 0.30	. . .
45 Aur................................	43905	57.0	8.14	0.84	. . .	. . .	. . .	. . .	. . .	. . .
η Aur..................................	32630	67.2	10.70	0.02	. . .	. . .	. . .	. . .	. . .	. . .
G191-B2B	. . .	68.8	8.61	0.74	17.4	4400^{+2800}_{-2400}	$3.27^{+0.37}_{-0.39}$	0.05 ± 0.11	0.87 ± 0.54	. . .

[a] Parameter $\sigma = (|v_0 - v_\star|)/\sigma_v$, where we have imposed a minimum σ_v of 1 km s^{-1} for all high-resolution data and a minimum σ_v of 3 km s^{-1} for all medium-resolution data.

[b] Other dynamical clouds for which the observed velocity is within 3 σ of the predicted value and the sight line is closer than 10° to the cloud. These are less likely but possible dynamical assignments for these sight lines.

TABLE 8
Mic Cloud Sight-Line Properties

Star Name	HD	d (pc)	v (km s^{-1})	σ[a]	log N(H I) (cm^{-2})	T (K)	ξ (km s^{-1})	D(Fe)	D(Mg)	Other Clouds[b]
α Aql......................	187642	5.1	-25.02	0.22	17.5	12500^{+2700}_{-2400}	$1.4^{+0.7}_{-1.4}$	-0.61 ± 0.23	-0.38 ± 0.24	. . .
α PsA	216956	7.7	-10.64	0.07	. . .	. . .	. . .	. . .	. . .	. . .
α Lyr	172167	7.8	-19.40	0.19	. . .	. . .	. . .	. . .	. . .	. . .
AU Mic	197481	9.9	-21.45	0.05	18.2	8700 ± 1200	4.30 ± 0.93	. . .	-0.55 ± 0.19	. . .
α Oph....................	159561	14.3	-26.23	0.05	. . .	. . .	. . .	. . .	. . .	G
99 Her	165908	15.7	-22.90	0.50	. . .	. . .	. . .	. . .	. . .	. . .
α CrB	139006	22.9	-17.40	0.21	. . .	. . .	. . .	. . .	. . .	Oph, Leo
β Cet	4128	29.4	1.63	0.15	16.9	12400 ± 2800	2.29 ± 0.44	. . .	0.23 ± 0.09	. . .
SAO 68491	184499	32.0	-19.73	0.74	. . .	. . .	. . .	. . .	. . .	. . .
λ Aql	177756	38.4	-26.50	1.38	. . .	. . .	. . .	. . .	. . .	G
β Ser......................	141003	46.9	-20.70	0.47	. . .	. . .	. . .	. . .	. . .	LIC, Oph, Leo
λ Oph	148857	50.9	-24.80	0.07	. . .	. . .	. . .	. . .	. . .	LIC, Oph
δ Cyg....................	186882	52.4	-16.30	0.27	. . .	. . .	. . .	. . .	. . .	. . .
ι Cap	203387	66.1	-20.48	0.41	18.1	11700^{+4100}_{-3600}	$3.82^{+0.37}_{-0.44}$	-1.22 ± 0.23	-0.47 ± 0.21	. . .
θ CrB....................	138749	95.3	-15.70	0.29	. . .	. . .	. . .	. . .	. . .	Oph

[a] Parameter $\sigma = (|v_0 - v_\star|)/\sigma_v$, where we have imposed a minimum σ_v of 1 km s^{-1} for all high-resolution data and a minimum σ_v of 3 km s^{-1} for all medium-resolution data.

[b] Other dynamical clouds for which the observed velocity is within 3 σ of the predicted value and the sight line is closer than 10° to the cloud. These are less likely but possible dynamical assignments for these sight lines.

TABLE 9
Oph Cloud Sight-Line Properties

Star Name	HD	d (pc)	v (km s^{-1})	σ[a]	$\log N$(H I) (cm^{-2})	T (K)	ξ (km s^{-1})	D(Fe)	D(Mg)	Other Clouds[b]
70 Oph	165341	5.1	−32.53	1.30	17.5	1700^{+2100}_{-1700}	3.3 ± 1.1	...	-0.84 ± 0.34	...
γ Ser	142806	11.1	−22.12	0.28	...	...	...	...	...	Mic
α Oph	159561	14.3	−28.40	1.17	...	...	...	...	...	G, Mic
72 Her	157214	14.4	−25.95	0.32	...	...	...	...	...	NGP
γ Oph	161868	29.1	−29.90	0.62	...	...	...	...	...	G, Mic
SAO 68491	184499	32.0	−27.85	0.02	...	...	...	...	...	...

[a] Parameter $\sigma = (|v_0 - v_\star|)/\sigma_v$, where we have imposed a minimum σ_v of 1 km s^{-1} for all high-resolution data and a minimum σ_v of 3 km s^{-1} for all medium-resolution data.

[b] Other dynamical clouds for which the observed velocity is within 3 σ of the predicted value and the sight line is closer than 10° to the cloud. These are less likely but possible dynamical assignments for these sight lines.

TABLE 10
Gem Cloud Sight-Line Properties

Star Name	HD	d (pc)	v (km s^{-1})	σ[a]	$\log N$(H I) (cm^{-2})	T (K)	ξ (km s^{-1})	D(Fe)	D(Mg)	Other Clouds[b]
ξ Boo A	131156	6.7	−17.69	0.33	17.9	5310 ± 830	1.68 ± 0.23	...	-0.92 ± 0.10	Mic, NGP
β Gem	62509	10.3	31.84	0.00	17.8	6100^{+3100}_{-2600}	$1.93^{+0.79}_{-0.59}$	-1.29 ± 0.12	-1.19 ± 0.14	...
α Boo	124897	11.3	−13.89	0.50	...	...	...	...	...	NGP
δ Crv	108767	26.9	−0.50	0.76	...	...	...	...	...	Aur
HR 4803	109799	34.6	−0.37	1.02	...	...	...	...	...	Aur
σ Gem	62044	37.5	32.26	0.55	17.7	7200^{+1000}_{-1200}	$0.0^{+1.1}_{-0.0}$	...	-1.18 ± 0.14	...
β Ser	141003	46.9	−23.30	1.61	...	...	...	...	...	Oph, NGP
β Lib	135742	49.1	−23.60	0.17	...	...	...	...	...	...
γ Crv	106625	50.6	1.60	0.73	...	...	...	...	...	...
c^2 Cen	129685	63.5	−16.90	0.36	...	...	...	...	...	...

[a] Parameter $\sigma = (|v_0 - v_\star|)/\sigma_v$, where we have imposed a minimum σ_v of 1 km s^{-1} for all high-resolution data and a minimum σ_v of 3 km s^{-1} for all medium-resolution data.

[b] Other dynamical clouds for which the observed velocity is within 3 σ of the predicted value and the sight line is closer than 10° to the cloud. These are less likely but possible dynamical assignments for these sight lines.

TABLE 11
NGP Cloud Sight-Line Properties

Star Name	HD	d (pc)	v (km s^{-1})	σ[a]	$\log N$(H I) (cm^{-2})	T (K)	ξ (km s^{-1})	D(Fe)	D(Mg)	Other Clouds[b]
61 Vir	115617	8.5	−16.50	0.01	17.9	<8500	...	...	...	Leo
α Oph	159561	14.3	−32.74	0.84	...	...	...	...	...	...
χ Her	142373	15.9	−12.90	0.76	18.2	<10200	...	...	...	Mic
ι Cen	115892	18.0	−18.20	0.31	...	...	...	...	...	G
SAO 28753	116956	21.9	3.20	0.57	18.2	<12600	...	...	...	LIC
ι Leo	99028	24.2	4.99	0.65	...	...	...	...	...	Leo
η UMa	120315	30.9	−3.02	0.11	17.9	8900^{+2500}_{-2300}	$1.34^{+0.24}_{-0.31}$	-0.93 ± 0.06	-0.78 ± 0.10	...
ι Dra	137759	31.3	−6.81	1.74	...	...	...	...	...	LIC
HZ 43	...	32.0	−6.52	0.40	18.0	7500^{+2100}_{-2000}	$1.7^{+0.8}_{-1.7}$	-1.42 ± 0.11	-1.08 ± 0.17	...
α^2 CVn	112413	33.8	−1.90	0.77	...	...	...	...	...	LIC
HR 4803	109799	34.6	−11.41	0.55	...	...	...	...	...	...
c^2 Cen	129685	63.5	−26.30	0.33	...	...	...	...	...	G
GD 153	...	70.5	−5.04	0.44	17.9	7000^{+2900}_{-2800}	$1.2^{+1.1}_{-1.2}$	-1.18 ± 0.13	...	...
31 Com	111812	94.2	−3.37	0.03	18.0	8200^{+1000}_{-1400}	$0.0^{+1.0}_{-0.0}$	-0.85 ± 0.15	-0.98 ± 0.14	...
θ CrB	138749	95.3	−19.90	0.72	...	...	...	...	...	Oph, Gem

[a] Parameter $\sigma = (|v_0 - v_\star|)/\sigma_v$, where we have imposed a minimum σ_v of 1 km s^{-1} for all high-resolution data and a minimum σ_v of 3 km s^{-1} for all medium-resolution data.

[b] Other dynamical clouds for which the observed velocity is within 3 σ of the predicted value and the sight line is closer than 10° to the cloud. These are less likely but possible dynamical assignments for these sight lines.

TABLE 12
Leo Cloud Sight-Line Properties

Star Name	HD	d (pc)	v (km s^{-1})	σ [a]	log N(H I) (cm^{-2})	T (K)	ξ (km s^{-1})	D(Fe)	D(Mg)	Other Clouds [b]
β Leo	102647	11.1	0.51	0.05	...	...	...	...	...	NGP
HR 4657	106516	22.6	−3.40	0.42	18.6	<27500	...	...	...	Aur, Gem, NGP
α Leo	87901	23.8	10.50	0.76	...	...	...	...	...	LIC
ι Leo	99028	24.2	1.97	0.50	...	...	...	...	...	...
HR 4803	109799	34.6	−7.52	0.40	...	...	...	...	...	...
β Ser	141003	46.9	−16.70	1.05	...	...	...	...	...	LIC
α Vir	116658	80.4	−11.99	0.80	...	...	...	...	...	...

[a] Parameter $\sigma = (|v_0 - v_\star|)/\sigma_v$, where we have imposed a minimum σ_v of 1 km s^{-1} for all high-resolution data and a minimum σ_v of 3 km s^{-1} for all medium-resolution data.
[b] Other dynamical clouds for which the observed velocity is within 3 σ of the predicted value and the sight line is closer than 10° to the cloud. These are less likely but possible dynamical assignments for these sight lines.

TABLE 13
Dor Cloud Sight-Line Properties

Star Name	HD	d (pc)	v (km s^{-1})	σ [a]	log N(H I) (cm^{-2})	T (K)	ξ (km s^{-1})	D(Fe)	D(Mg)	Other Clouds [b]
ζ Dor	33262	11.7	13.90	0.35	18.1	7000^{+3500}_{-3000}	$5.47^{+0.39}_{-0.41}$	−0.80 ± 0.30	−0.65 ± 0.31	...
τ^6 Eri	23754	17.9	41.40	0.12	...	...	...	...	...	...
ϵ Gru	215789	39.7	12.20	0.66	...	...	...	...	...	...
α Eri	10144	44.1	21.20	0.24	...	...	...	...	...	...

[a] Parameter $\sigma = (|v_0 - v_\star|)/\sigma_v$, where we have imposed a minimum σ_v of 1 km s^{-1} for all high-resolution data and a minimum σ_v of 3 km s^{-1} for all medium-resolution data.
[b] Other dynamical clouds for which the observed velocity is within 3 σ of the predicted value and the sight line is closer than 10° to the cloud. These are less likely but possible dynamical assignments for these sight lines.

TABLE 14
Vel Cloud Sight-Line Properties

Star Name	HD	d (pc)	v (km s^{-1})	σ [a]	log N(H I) (cm^{-2})	T (K)	ξ (km s^{-1})	D(Fe)	D(Mg)	Other Clouds [b]
AB Dor	36705	14.9	14.22	0.11	...	...	...	...	...	Cet
SAO 254993	254993	20.5	−13.10	1.24	18.8	<23000	...	...	...	LIC, G
α Hyi	12311	21.9	9.80	0.31	...	...	...	...	...	...
δ Vel	74956	24.4	11.80	0.18	...	...	...	...	...	...
α Eri	10144	44.1	11.00	0.45	...	...	...	...	...	...
BO Mic	197890	44.4	−24.20	0.28	18.3	10600 ± 2700	3.48 ± 1.87	...	−0.03 ± 0.72	Mic
α Pav	193924	56.2	−19.60	0.63	...	...	...	...	...	...

[a] Parameter $\sigma = (|v_0 - v_\star|)/\sigma_v$, where we have imposed a minimum σ_v of 1 km s^{-1} for all high-resolution data and a minimum σ_v of 3 km s^{-1} for all medium-resolution data.
[b] Other dynamical clouds for which the observed velocity is within 3 σ of the predicted value and the sight line is closer than 10° to the cloud. These are less likely but possible dynamical assignments for these sight lines.

TABLE 15
Cet Cloud Sight-Line Properties

Star Name	HD	d (pc)	v (km s^{-1})	σ [a]	log N(H I) (cm^{-2})	T (K)	ξ (km s^{-1})	D(Fe)	D(Mg)	Other Clouds [b]
σ Boo	128167	15.5	−12.90	1.10	...	...	...	...	...	...
δ Vel	74956	24.4	15.60	0.79	...	...	...	...	...	...
β Cet	4128	29.4	9.14	0.53	18.5	6300 ± 2900	1.31 ± 0.76	...	0.21 ± 0.33	LIC
HR 4023	88955	31.5	10.50	0.48	...	...	...	...	...	...
α Eri	10144	44.1	7.60	1.80	...	...	...	...	...	G, Vel

[a] Parameter $\sigma = (|v_0 - v_\star|)/\sigma_v$, where we have imposed a minimum σ_v of 1 km s^{-1} for all high-resolution data and a minimum σ_v of 3 km s^{-1} for all medium-resolution data.
[b] Other dynamical clouds for which the observed velocity is within 3 σ of the predicted value and the sight line is closer than 10° to the cloud. These are less likely but possible dynamical assignments for these sight lines.

TABLE 16
LISM Cloud Heliocentric Velocity Vectors

Cloud Name	Number of Sight Lines	V_0 (km s^{-1})	l_0 (deg)	b_0 (deg)	χ^2_ν
LIC...	79	23.84 ± 0.90	187.0 ± 3.4	-13.5 ± 3.3	2.2
G..	21	29.6 ± 1.1	184.5 ± 1.9	-20.6 ± 3.6	1.3
Blue.......................................	10	13.89 ± 0.89	205.5 ± 4.3	-21.7 ± 8.3	2.4
Aql...	9	58.6 ± 1.3	187.0 ± 1.5	-50.8 ± 1.0	2.6
Eri..	8	24.1 ± 1.2	196.7 ± 2.1	-17.7 ± 2.6	0.3
Aur	9	25.22 ± 0.81	212.0 ± 2.4	-16.4 ± 3.6	2.1
Hyades....................................	14	14.69 ± 0.81	164.2 ± 9.4	-42.8 ± 6.1	1.3
Mic...	15	28.45 ± 0.95	203.0 ± 3.4	-03.3 ± 2.3	0.5
Oph..	6	32.25 ± 0.49	217.7 ± 3.1	$+00.8 \pm 1.8$	3.9
Gem..	10	36.3 ± 1.1	207.2 ± 1.6	-01.2 ± 1.3	1.7
NGP..	15	37.0 ± 1.4	189.8 ± 1.7	-05.4 ± 1.1	3.8
Leo	7	23.5 ± 1.6	191.3 ± 2.8	-08.9 ± 1.8	1.5
Dor...	4	52.94 ± 0.88	157.3 ± 1.5	-47.93 ± 0.63	0.8
Vel	7	45.2 ± 1.8	195.4 ± 1.1	-19.1 ± 1.0	0.8
Cet...	5	60.0 ± 2.0	197.11 ± 0.56	-08.72 ± 0.50	8.9
LIC[a].....................................	9	25.7 ± 0.5	186.1	-16.4	...
LIC[b].....................................	16	26 ± 1	186 ± 3	-16 ± 3	...
LIC[c].....................................	63	24.20 ± 1.05	187.0 ± 3.1	-13.5 ± 3.0	2.1
G[a]	...	29.4	185.5	-20.5	...
Helio[d]	...	26.24 ± 0.45	183.4 ± 0.4	-15.9 ± 0.4	...
(LIC+G)/2[e]	...	26.74 ± 0.71	185.7 ± 3.4	-16.95 ± 3.6	...

[a] Lallement & Bertin (1992).
[b] Lallement et al. (1995).
[c] LIC flow vector deleting the 16 lines of sight near the decelerated leading edge of the LIC in the direction of the Hyades Cloud.
[d] Flow vector for interstellar helium gas in the heliosphere. Temperature is 6303 ± 390 K (Möbius et al. 2004). See temperatures for individual dynamical clouds in Table 18.
[e] Average of the LIC and G vectors. Average temperature of the LIC and G Cloud is 6500 ± 680 K. The in situ "Helio" measurement is closer to the average LIC and G temperature than either cloud individually; see Table 18.
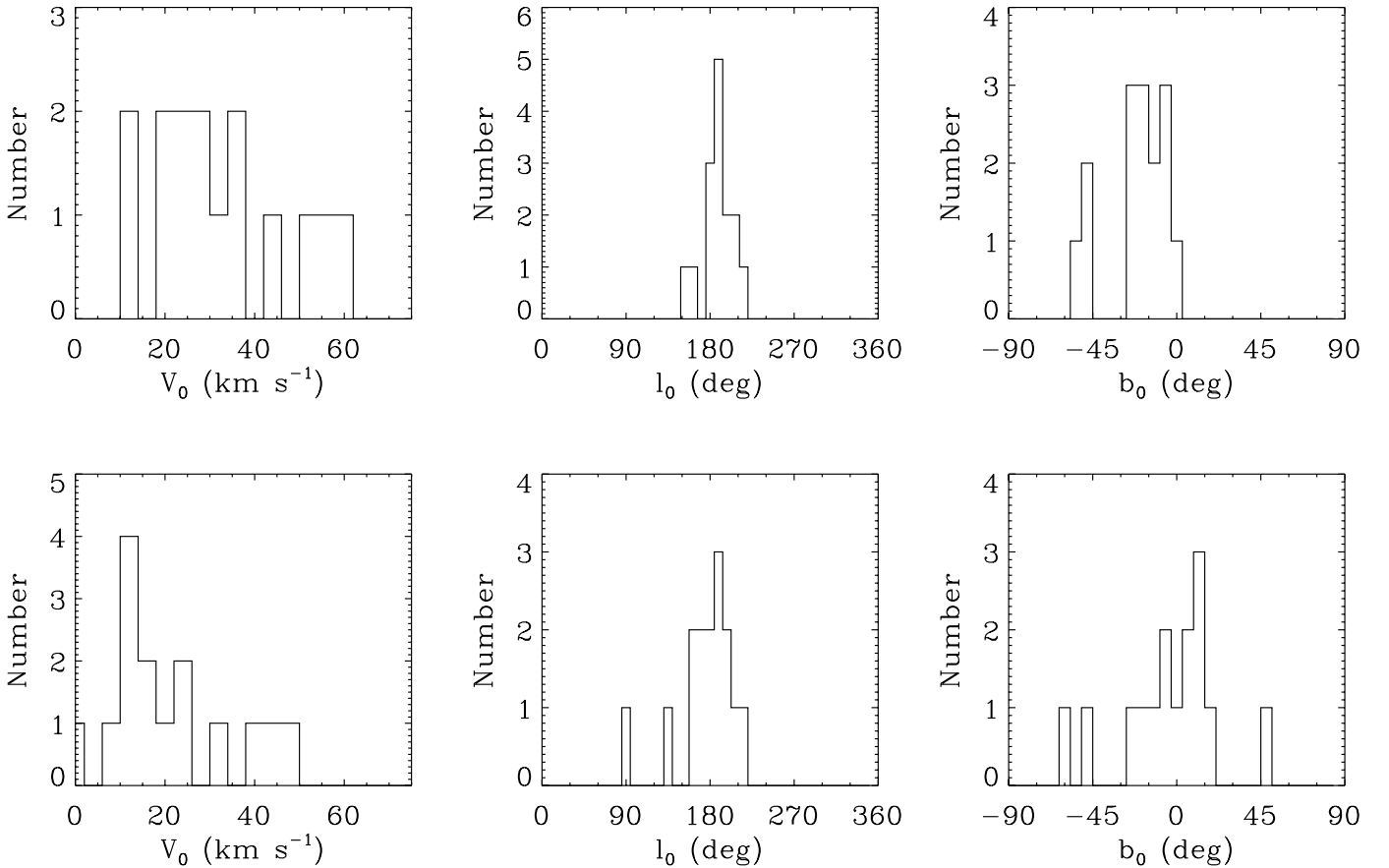

Fig. 16.—Distributions of fit parameters, downwind heliocentric (top) velocity (V_0), and direction in Galactic coordinates (l_0, b_0) for 15 clouds identified within 15 pc. The distribution of downwind velocity and direction relative to the LSR is shown in the bottom panels, where the upstream solar motion relative to the LSR ($V_\odot = 13.4$ km s^{-1}, $l_\odot = 207.7°$, $b_\odot = -32.4°$) was derived by Dehnen & Binney (1998). The bin sizes are 4 km s^{-1} in V_0, 9° in l_0, and 6° in b_0. All velocity vectors appear to be driven in the same direction, although at a range of velocities.
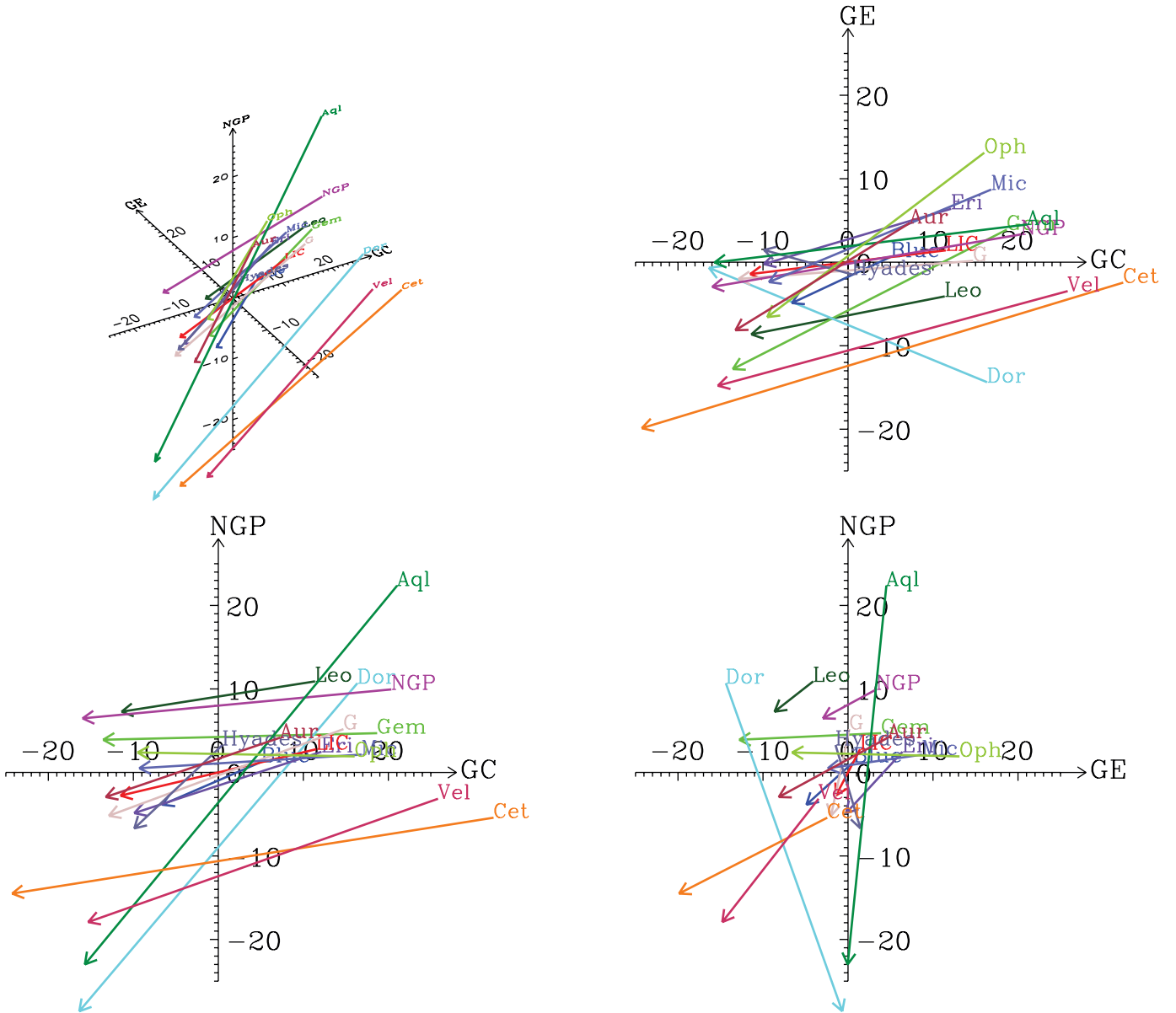
Fig. 17.—Heliocentric velocity vectors of all 15 clouds. The vectors are centered in the direction of the center of the cloud and at the distance of the closest star with the cloud's absorption velocity and point downwind. The Sun is moving in roughly the opposite direction as the LISM clouds. Starting from the top left and moving clockwise, the plots are viewed from $l = 230°$ and $b = 45°$, the north Galactic pole ($b = 90°$), the Galactic center ($l = 0°$ and $b = 0°$), and Galactic east ($l = 90°$ and $b = 0°$).

increasing $N(\text{H I})$ and toward the crosswind direction where the two clouds meet. The turbulent velocities do not show a definite trend with angle or $N(\text{H I})$. If there were a velocity gradient through these clouds, one would expect larger line broadening (and thus higher turbulent velocity) in the downwind and upwind directions, which is not seen. Finally, the metal depletions [$D(\text{Mg})$ and $D(\text{Fe})$] show clear trends of decreasing with larger $N(\text{H I})$ and increasing with angle, with both the LIC and G Cloud sight lines fitting these trends. On average, the LIC is significantly more depleted than the G Cloud. The trend of decreasing gas-phase abundances as a function of increasing $N(\text{H I})$ is well documented along distant sight lines (e.g., Wakker & Mathis 2000; Jenkins et al. 1986). This implies that the processes that remove and replace ions to the gas phase occur on scales smaller than the LIC and G Cloud and that the volume density of the LIC and G Cloud may not be constant. Alternatively, decreasing $D(\text{Mg})$ and $D(\text{Fe})$ with increasing $N(\text{H I})$ may be explained if H I is photoionized at the edges of clouds and

is increasingly neutral with increasing H I through the centers of clouds due to shielding of UV radiation from the cloud itself. Thus, while the fraction of magnesium and iron in the gas phase relative to the total amount of hydrogen remains the same throughout, $D(\text{Mg})$ and $D(\text{Fe})$ will decrease as hydrogen becomes predominately neutral. On the basis of the temperature and turbulent velocity data, we conclude that the evidence supports the idea that the LIC and G Cloud are separate entities with their own distinct properties, but there is likely a narrow transition zone between the two clouds where the heliosphere is now located.

6. CONCLUSIONS

We have created a database consisting of interstellar radial velocities and gas physical properties for 157 sight lines toward stars within 100 pc of the Sun. The data were extracted from high-resolution UV spectra obtained with the GHRS and STIS instruments on the *HST* and ground-based Ca II spectra. This database

TABLE 17
Unassigned Sight-Line Properties

Star Name	HD	d (pc)	v (km s^{-1})	log N(H I) (cm^{-2})	T (K)	ξ (km s^{-1})	D(Fe)	D(Mg)	Possible Clouds[a]
AD Leo	. . .	4.7	13.13	18.5	<12300	. . .	. . .	. . .	LIC, Leo
η Cas A	4614	6.0	5.80	. . .	. . .	. . .	. . .	. . .	. . .
κ^1 Cet	20630	9.2	7.36	17.4	5800 ± 2700	1.48 ± 0.92	. . .	−1.51 ± 0.23	. . .
β Leo	102647	11.1	11.80	. . .	. . .	. . .	. . .	. . .	. . .
AB Dor	36705	14.9	19.38	. . .	. . .	. . .	. . .	. . .	. . .
τ^6 Eri	23754	17.9	27.93	. . .	. . .	. . .	. . .	. . .	. . .
			8.82	. . .	. . .	. . .	. . .	. . .	. . .
PW And	1405	21.9	2.00	. . .	. . .	. . .	. . .	. . .	LIC, Eri
SAO 158720	128987	23.6	−22.00	18.1	<12400	. . .	. . .	. . .	G, Gem, NGP, Leo
δ Her	156164	24.1	−19.50	. . .	. . .	. . .	. . .	. . .	LIC
SAO 32862	198084	27.1	−12.88	. . .	. . .	. . .	. . .	. . .	. . .
HR 1099	22468	29.0	8.20	17.2	7100 ± 1400	2.30 ± 0.25	. . .	−1.21 ± 0.12	. . .
γ Oph	161868	29.1	−33.00	. . .	. . .	. . .	. . .	. . .	Oph, NGP
α And	358	29.8	13.00	. . .	. . .	. . .	. . .	. . .	Hyades
η UMa	120315	30.9	2.60	16.6	0^{+4400}_{-0}	$5.6^{+0.9}_{-1.1}$	. . .	−0.78 ± 0.15	NGP
α Gru	209952	31.1	−6.40	. . .	. . .	. . .	. . .	. . .	LIC, Vel
			−21.40	. . .	. . .	. . .	. . .	. . .	LIC, Vel
σ Gem	62044	37.5	21.77	17.9	8600 ± 1600	2.46 ± 0.45	. . .	−0.92 ± 0.14	LIC
HR 2298	44769	39.4	7.00	. . .	. . .	. . .	. . .	. . .	. . .
ϵ Gru	215789	39.7	6.80	. . .	. . .	. . .	. . .	. . .	. . .
			−1.70	. . .	. . .	. . .	. . .	. . .	. . .
			−12.30	. . .	. . .	. . .	. . .	. . .	. . .
			−22.40	. . .	. . .	. . .	. . .	. . .	. . .
SAO 93981	28568	41.2	16.50	. . .	. . .	. . .	. . .	. . .	Hyades
SAO 111879	28736	43.2	−4.30	. . .	. . .	. . .	. . .	. . .	. . .
SAO 93982	28608	43.6	15.80	. . .	. . .	. . .	. . .	. . .	Hyades
α Eri	10144	44.1	18.90	. . .	. . .	. . .	. . .	. . .	Dor
SAO 93945	28237	47.2	15.60	. . .	. . .	. . .	. . .	. . .	Hyades
β Lib	135742	49.1	−33.70	. . .	. . .	. . .	. . .	. . .	. . .
SAO 94162	30738	51.8	20.30	. . .	. . .	. . .	. . .	. . .	Aur
κ And	222439	52.0	0.80	. . .	. . .	. . .	. . .	. . .	. . .
υ Peg	220657	53.1	−7.48	17.4	3600^{+4400}_{-3000}	$1.7^{+0.7}_{-1.5}$	−0.83 ± 0.2	−0.54 ± 0.21	. . .
SAO 93913	27848	53.4	16.40	. . .	. . .	. . .	. . .	. . .	Aur, Hyades
HR 1608	32008	54.7	6.10	17.7	<11500	. . .	. . .	. . .	Blue, Hyades
α Pav	193924	56.2	−18.60	. . .	. . .	. . .	. . .	. . .	Vel
η Aqr	213998	56.3	−2.10	. . .	. . .	. . .	. . .	. . .	LIC
SAO 159459	140283	57.3	−22.48	. . .	. . .	. . .	. . .	. . .	Gem, Leo
ι Cap	203387	66.1	−2.22	18.4	5500^{+10600}_{-5500}	$3.7^{+0.7}_{-1.1}$	−0.63 ± 0.37	−0.28 ± 0.38	. . .
η Aur	32630	67.2	6.80	. . .	. . .	. . .	. . .	. . .	. . .
ι Oph	152614	71.7	−11.00	. . .	. . .	. . .	. . .	. . .	. . .
			−30.80	. . .	. . .	. . .	. . .	. . .	NGP
Feige 24	. . .	74.4	3.10	18.2	. . .	. . .	. . .	. . .	. . .
γ Ori	35468	74.5	16.00	. . .	. . .	. . .	. . .	. . .	. . .
			20.20	. . .	. . .	. . .	. . .	. . .	. . .
			27.80	. . .	. . .	. . .	. . .	. . .	. . .
α Vir	116658	80.4	−5.40	. . .	. . .	. . .	. . .	. . .	Gem
			−3.68	. . .	. . .	. . .	. . .	. . .	. . .
θ Aql	191692	88.0	−22.60	. . .	. . .	. . .	. . .	. . .	Mic
τ Her	147394	96.4	−33.50	. . .	. . .	. . .	. . .	. . .	. . .
			−38.00	. . .	. . .	. . .	. . .	. . .	. . .
HD 141569	141569	99.0	−13.70	. . .	. . .	. . .	. . .	. . .	. . .

[a] Although they do not fit the criteria for membership in any of the dynamical clouds, we list here possible membership where the observed velocity is within 3 σ of a predicted cloud value and the sight line is closer than 10° to the cloud.

TABLE 18
SUMMARY OF CLOUD PROPERTIES

Cloud Name	Number of Sight Lines	Central Coordinates		Closest Star (pc)	Surface Area (deg²)	⟨T⟩ (K)	Number of Stars	⟨ξ⟩ (km s⁻¹)	Number of Sight Lines	⟨D(Fe)⟩	Number of Sight Lines	⟨D(Mg)⟩	Number of Sight Lines	Morphology
		l (deg)	b (deg)											
LIC	79	170	−10	2.6	18270	7500 ± 1300	19	1.62 ± 0.75	19	−1.12 ± 0.10	12	−0.97 ± 0.23	21	Compact
G	21	315	+00	1.3	8230	5500 ± 400	5	2.2 ± 1.1	5	−0.54 ± 0.11	4	−0.36 ± 0.35	5	Compact
Blue	10	250	−30	2.6	2310	3900 ± 2300	3	2.64 ± 0.16	3	−0.84 ± 0.27	2	−0.51 ± 0.49	2	Compact
Aql	9	40	−05	3.5	2960	7000 ± 2800	3	2.07 ± 0.64	3	(−0.96)[a]	1	−0.69 ± 0.21	3	Compact
Eri	8	70	−20	3.5	1970	5300 ± 4000	3	3.6 ± 1.0	3	−0.39 ± 0.19	2	−0.15 ± 0.30	3	Compact
Aur	9	210	+10	3.5	1640	(6710)[a]	1	(1.2)[a]	1	(−1.13)[a]	1	(−0.79)[a]	1	Filamentary
Hyades	14	180	−20	5.0	1810	6200 ± 3800	5	2.7 ± 1.2	5	−0.32 ± 0.62	4	−1.06 ± 0.47	5	Filamentary
Mic	15	40	+15	5.1	3550	9900 ± 2000	4	3.1 ± 1.0	4	−0.92 ± 0.43	2	−0.03 ± 0.40	4	Filamentary
Oph	6	45	+25	5.1	1360	(1700)[a]	1	(3.3)[a]	1	...	0	(−0.84)[a]	1	Compact
Gem	10	300	+40	6.7	3300	6000 ± 1100	3	1.63 ± 0.41	3	(−1.29)[a]	1	−1.05 ± 0.16	3	Filamentary
NGP	15	5	+75	8.5	4020	8000 ± 600	4	1.23 ± 0.43	4	−1.04 ± 0.23	4	−0.89 ± 0.15	3	Compact
Leo	7	270	+55	11.1	2400	...	0	...	0	...	0	...	0	Compact
Dor	4	270	−50	11.7	1550	(7000)[a]	1	(5.5)[a]	1	(−0.80)[a]	1	(−0.65)[a]	1	Compact
Vel	7	300	−45	14.9	2190	(10600)[a]	1	(3.5)[a]	1	...	0	(−0.03)[a]	1	Compact
Cet	5	290	−40	15.5	2270	(6300)[a]	1	(1.3)[a]	1	...	0	(0.21)[a]	1	Filamentary

[a] Those clouds with only one sight line with a physical measurement are indicated in parentheses. Since a weighted average is not possible, the listed properties should be considered uncertain.
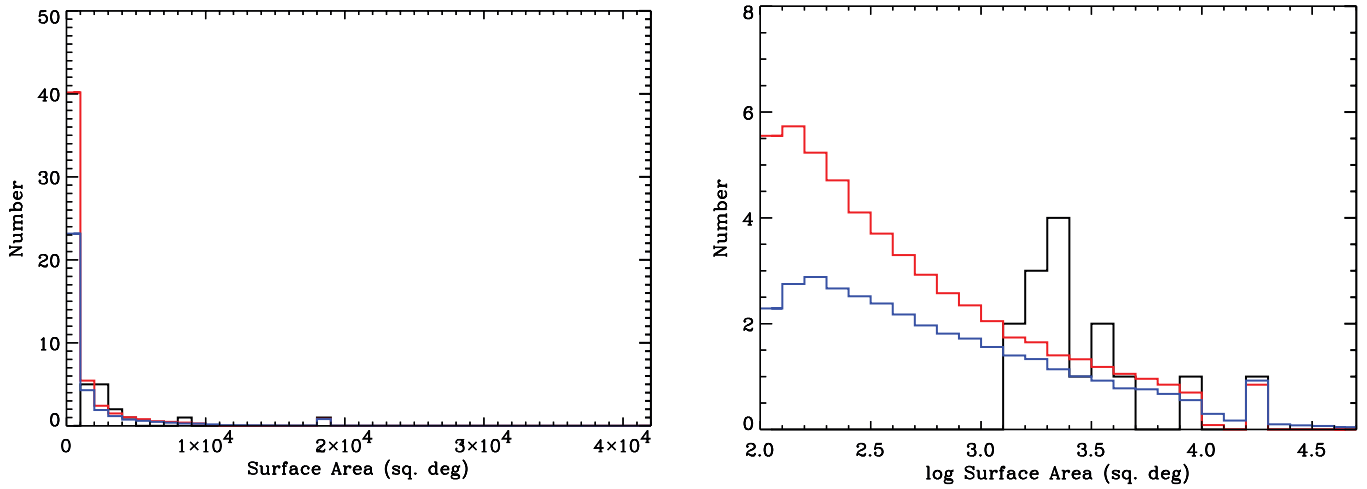
Fig. 18.— Histogram (*black*) of the observed angular areas of the 15 nearby dynamical clouds, based on their projected morphologies shown in Figs. 1–15. The histograms on the left have bin sizes of $1000 \deg^2$, while the histograms on the right have bin sizes of 0.1 dex in logarithmic square degrees. The red histogram indicates the average distribution of angular areas of the simple model of 55 randomly distributed spherical LIC-like clouds within 15 pc of the Sun, discussed in § 4.2. This model leads to a volume filling factor of ∼5.5%. The blue histogram shows another simple simulation of 35 randomly oriented clouds, in which half were ellipsoids with aspect ratios of 10 : 1. Although this simulation also reproduces the observed projected surface areas of the 15 large clouds fairly well, the volume filling factor in this case is ∼19%.
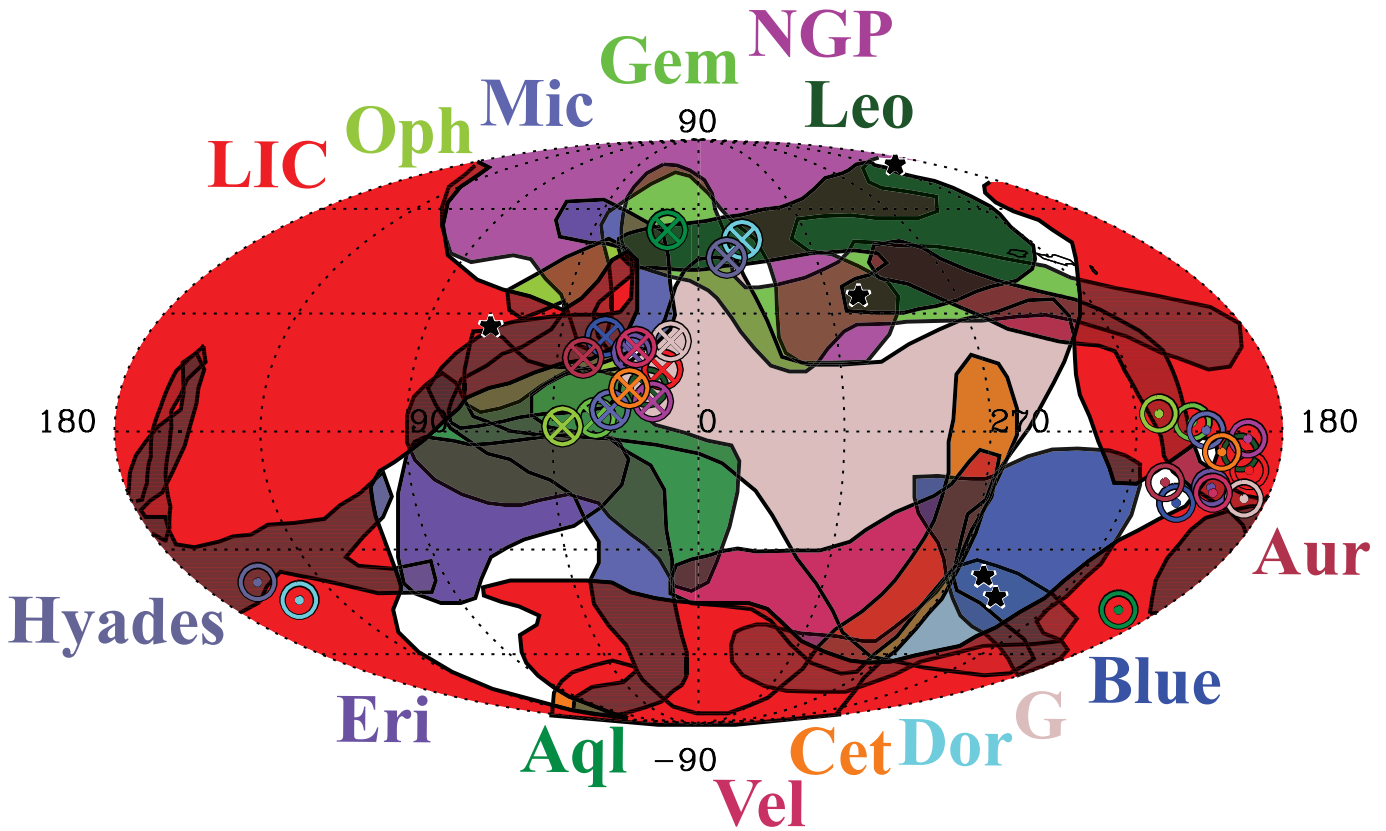
Fig. 19.— All dynamical cloud morphologies are overlaid and color-coded as in Fig. 17. The upwind heliocentric direction of the velocity vector for each cloud is indicated by the circled cross, while the downwind heliocentric direction is indicated by the circled dot. The Sun is moving approximately antiparallel to the LISM clouds. The stars indicate sight lines of radio scintillation sources, and the series of three small clouds centered at $l = 222°$ and $b = 44°$ are the H I contours from Heiles & Troland (2003) of the cold cloud recently identified to be within the LB by Meyer et al. (2006).

310

FIG. 22.—Distribution of cloud velocity differences between all 15 LISM clouds shown here for all sight lines that are predicted to traverse multiple clouds based on the spatial distribution of clouds shown in Fig. 19. The predicted velocity components of all 15 clouds were calculated for a uniform sample of hypothetical lines of sight over the full sky. Velocity differences between the LIC and G Cloud in directions in which both are observed are indicated by the red histograms. The mean thermal sound speed is ~8 km s^{-1}. A significant fraction of possible velocity differences between LISM clouds include velocities greater than the thermal sound speed. Distributions in the radial (*top*) and transverse (*l, middle; b, bottom*) Galactic directions are shown. The blue histogram (scaled by a factor of 50) represents the macroscopic velocity differences for LISM material near the Leo cold cloud. Significant compressional velocities of the warm LISM material in the radial direction may be a mechanism for the origin of the cold dense material observed by Meyer et al. (2006).

FIG. 20.—Two subsets of dynamical cloud morphologies are overlaid and color-coded as in Fig. 17. The upwind heliocentric direction of the velocity vectors is indicated by the circled cross, while the downwind heliocentric direction is indicated by the circled dot. The top panel shows the projected morphological similarities shared by the LIC, G Cloud, and Mic Cloud, indicating that clouds like the Mic could result from collisions of other clouds, in this case the LIC and G Cloud. The bottom panel shows the clouds in close angular proximity to the cold cloud (shown here are H I contours from Heiles & Troland [2003], which are the series of three small clumps centered at $l = 222°$ and $b = 44°$), which was identified to be within the LB by Meyer et al. (2006). Note that the alignment of the cold cloud matches well with the alignment of the high-velocity Gem Cloud in the same location. The compressional macroscopic motions between the surrounding warm dynamical clouds (e.g., the Gem Cloud with the slower moving Leo Cloud, Aur Cloud, and LIC) shown here may be the origin mechanism of the observed cold material.

FIG. 21.—Distribution of the weighted mean values of turbulent velocity (ξ) and depletion of iron [$D(Fe)$] and magnesium [$D(Mg)$] for all clouds with more than one sight line having a turbulent velocity measurement. The errors are the dispersion about the weighted mean. The dashed line is a weighted minimum χ^2 linear fit to the data. A clear correlation exists between cloud turbulent velocity and depletion for both elements, with a linear correlation coefficient $r = 0.69$ and a probability that the distribution could be drawn from an uncorrelated parent population of only $P_c = 1.7\%$ for iron and $r = 0.73$ and $P_c = 1.2\%$ for magnesium. It is likely that regions of high turbulence result from the dynamical interactions of clouds, which in turn produce shocks and heat any dust, returning metal ions from the dust to the gas phase.
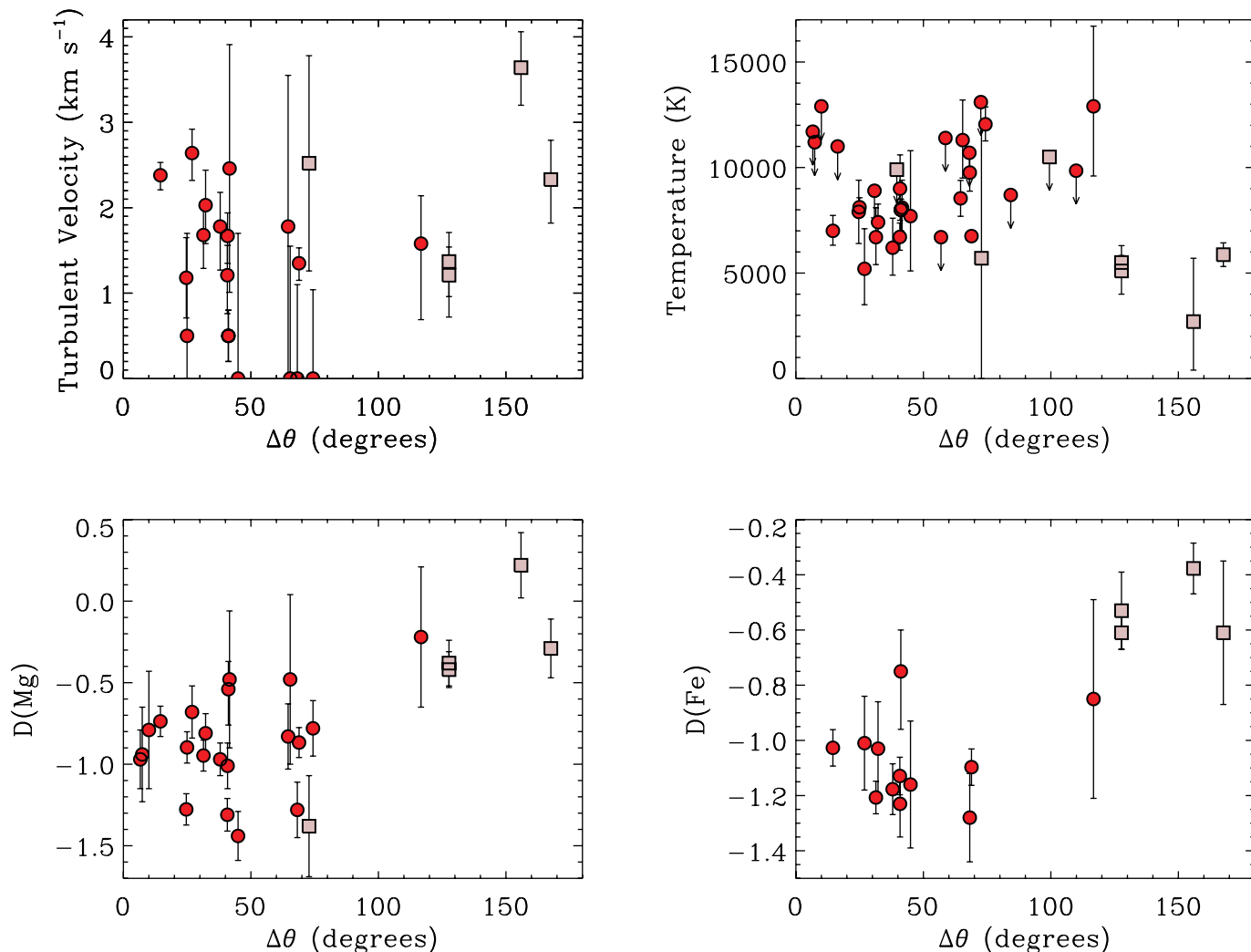
311

FIG. 23.—Comparison of LIC and G sight-line physical properties as a function of angular distance from the LIC downwind direction. Sight lines through each cloud are distinguished by color (*red*: LIC; *pale pink*: G) and symbol (*circle*: LIC; *square*: G). Since the G Cloud is in the upstream direction, all G Cloud sight lines are at high $\Delta\theta$. Except for one LIC value, all temperatures through the LIC are higher than the G Cloud temperatures. A correlation with angle is evident in the depletion of magnesium ($r = 0.63$, $P_c = 0.012\%$) and iron ($r = 0.80$, $P_c = 0.0041\%$).

has allowed us to create a dynamical model of the LISM[8] including 15 warm gas clouds, which we define as contiguous parcels of interstellar gas with consistent kinematical properties. Although measurements of physical properties are sparse, for the LIC, which has the most such measurements, the properties seem to be homogeneous. Using this database, we find the following:

1. The flow velocity vectors for these 15 clouds fit 81.2% of the velocity components in the database to within the radial velocity measurement errors. These clouds all lie within 15 pc of the Sun. The remaining velocity components may be produced in more distant clouds that subtend smaller angles with less than the four lines of sight needed to compute a useful velocity vector.

2. The directions of most of these velocity vectors are roughly parallel with their flow from the Scorpio-Centaurus association. The velocity amplitudes have a considerable range, leading us to compute relative velocities between adjacent clouds that are often supersonic and therefore capable of producing shocks.

3. About one-third of the clouds appear to have filamentary structures.

4. All of the clouds for which we have physical properties along three or more sight lines are warm, with mean temperatures in the range of 5300–9900 K, although the uncertainties in these measurements are often large. We estimate that between 5.5% and 19% of the LISM within 15 pc of the Sun is filled with warm gas clouds.

5. We find a strong correlation of low metal depletion with large turbulent velocity. Since high turbulence suggests the presence or recent existence of shocks, this correlation could be explained by shock dissipation of dust grains that returns the metals to the gas phase.

6. Contrary to previous work, the heliosphere appears to be located in a transition zone between the LIC and G Cloud. The evidence for this is that the temperature and velocity of the interstellar gas flowing through the heliosphere are both intermediate between these quantities measured in the LIC and G Cloud. The deviation in velocity ranges from 2.4 to 2.9 σ, and in temperature the deviation is less significant, ranging from 0.9 to 1.4 σ. Additional observations of multiple ions are required to increase the number of temperature measurements of the LIC and G Cloud in

---

[8] Projected and transverse velocities, along with probable cloud membership based on the projected cloud morphologies, can be calculated for any sight line at http://cobalt.as.utexas.edu/~sredfield/LISMdynamics.html.
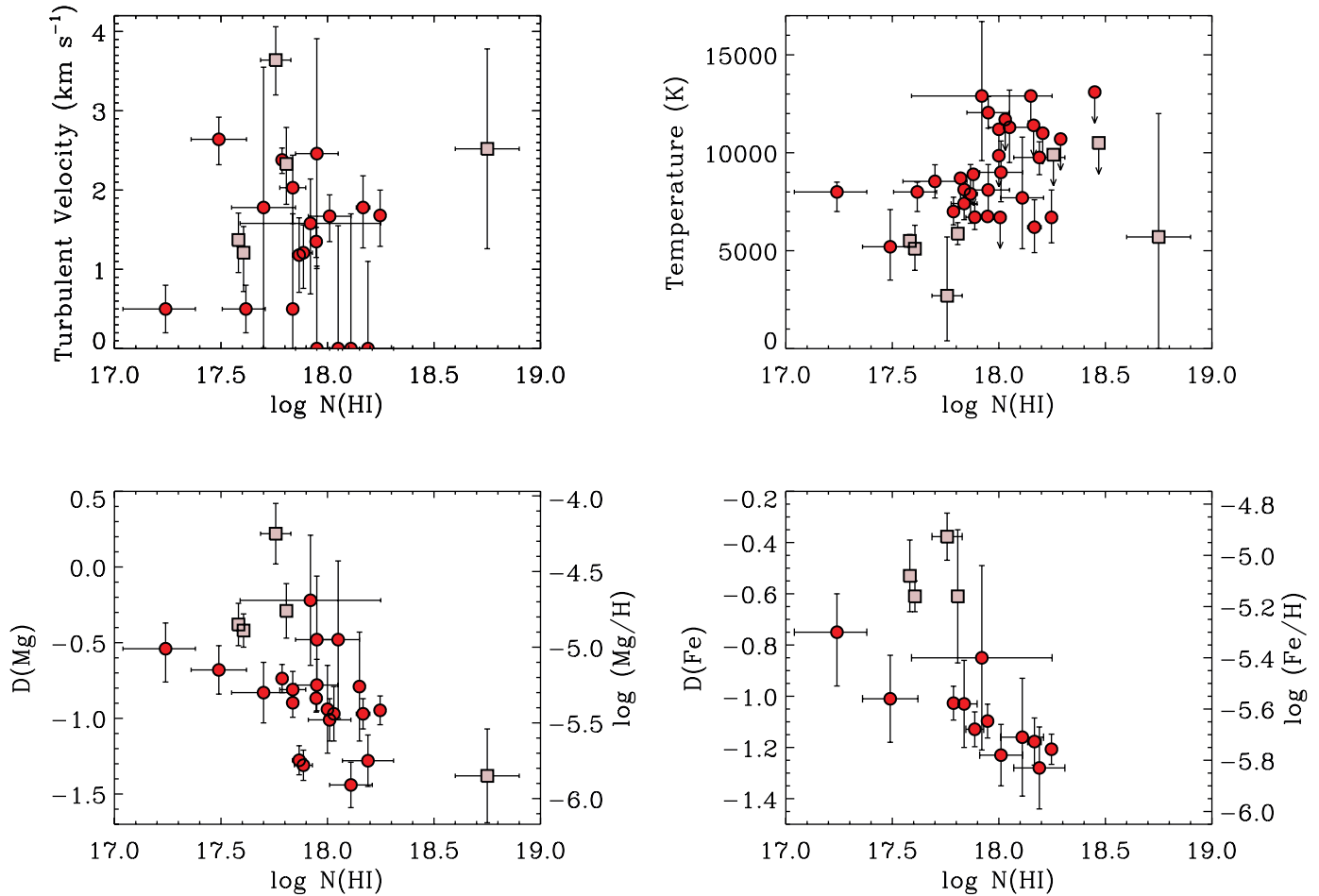
FIG. 24.—Similar to Fig. 23, but the comparison of LIC and G sight-line physical properties is shown as a function of hydrogen column density. Correlations are seen between hydrogen column density and depletion of magnesium ($r = -0.53$, $P_c = 0.12\%$) and iron ($r = -0.65$, $P_c = 0.15\%$).

order to increase the significance of any possible deviation between these clouds and in situ measurements. Previous work based on much smaller velocity data sets placed the heliosphere inside but near the edge of the LIC.

7. The G Cloud is surrounded by and likely interacting with a number of other clouds. We refer to this active boundary as the "Ring of Fire." The filamentary-shaped Mic Cloud has the same shape as the boundary of the G Cloud and LIC and may be indicative of an interaction between these two clouds. The high temperature and turbulence of the Mic Cloud support this conclusion.

8. The nearby scintillation screens toward three quasars and two pulsars are located near cloud boundaries, and three of the five are in directions where the LIC and G Cloud may be interacting. The large transverse relative velocities between these two clouds could produce the turbulence that is the cause of the scintillation.

9. The nearby cold cloud recently observed by Heiles & Troland (2003) and Meyer et al. (2006) is in a direction where it could be surrounded by several warm clouds. We find evidence for significant compression based on large macroscopic velocity differences between warm clouds in the direction of the cold cloud. The alignment of the cold cloud matches well with the alignment of the high-velocity Gem Cloud, which may be colliding with

the slower moving Leo, Aur, and LIC Clouds. Compression of warm material may be the origin mechanism for such an isolated cold cloud in the LB.

Facilities: HST (GHRS, STIS)

REFERENCES

Asplund, M., Grevesse, N., & Sauval, A. J. 2005, in ASP Conf. Ser. 336, Cosmic Abundances as Records of Stellar Evolution and Nucleosynthesis in Honor of David L. Lambert, ed. T. G. Barnes & F. N. Bash (San Francisco: ASP), 25

Audit, E., & Hennebelle, P. 2005, A&A, 433, 1

Bannister, N. P., Barstow, M. A., Holberg, J. B., & Bruhweiler, F. C. 2003, MNRAS, 341, 477

Baranov, V. B. 1990, Space Sci. Rev., 52, 89

Berghöfer, T. W., & Breitschwerdt, D. 2002, A&A, 390, 299

Bevington, P. R., & Robinson, D. K. 1992, Data Reduction and Error Analysis for the Physical Sciences (2nd ed.; New York: McGraw-Hill)

Bignall, H. E., Macquart, J.-P., Jauncey, D. L., Lovell, J. E. J., Tzioumis, A. K., & Kedziora-Chudczer, L. 2006, ApJ, 652, 1050

Blades, J. C., Wynne-Jones, I., & Wayte, R. C. 1980, MNRAS, 193, 849

Brandeker, A., Liseau, R., Olofsson, G., & Fridlund, M. 2004, A&A, 413, 681

Cox, D. P. 2005, ARA&A, 43, 337

Cox, D. P., & Helenius, L. 2003, ApJ, 583, 205

Crawford, I. A., & Dunkin, S. K. 1995, MNRAS, 273, 219

Crutcher, R. M. 1982, ApJ, 254, 82

Dehnen, W., & Binney, J. J. 1998, MNRAS, 298, 387

Dennett-Thorpe, J., & de Bruyn, A. G. 2003, A&A, 404, 113

Dupuis, J., Vennes, S., Bowyer, S., Pradhan, A. K., & Thejll, P. 1995, ApJ, 455, 574

Field, G. B., Goldsmith, D. W., & Habing, H. J. 1969, ApJ, 155, L149

France, K., Roberge, A., Lupu, R. E., Redfield, S., & Feldman, P. D. 2007, ApJ, 668, 1174

Frisch, P. C., ed. 2006, Solar Journey: The Significance of our Galactic Environment for the Heliosphere and Earth (Dordrecht: Springer)

Frisch, P. C., Grodnicki, L., & Welty, D. E. 2002, ApJ, 574, 834

Frisch, P. C., & York, D. G. 1983, ApJ, 271, L59

Frisch, P. C., et al. 1999, ApJ, 525, 492

Génova, R., & Beckman, J. E. 2003, ApJS, 145, 355

Gloeckler, G., et al. 2004, A&A, 426, 845

Graham, J. R., Levenson, N. A., Hester, J. J., Raymond, J. C., & Petre, R. 1995, ApJ, 444, 787

Gry, C., Lemonon, L., Vidal-Madjar, A., Lemoine, M., & Ferlet, R. 1995, A&A, 302, 497

Hébrard, G., Mallouris, C., Ferlet, R., Koester, D., Lemoine, M., Vidal-Madjar, A., & York, D. 1999, A&A, 350, 643

Heiles, C., & Troland, T. H. 2003, ApJ, 586, 1067

Hobbs, L. M., Vidal-Madjar, A., Ferlet, R., Albert, C. E., & Gry, C. 1985, ApJ, 293, L29

Jackson, T., Werner, M., & Gautier, T. N., III. 2003, ApJS, 149, 365

Jauncey, D. L., Johnston, H. M., Bignall, H. E., Lovell, J. E. J., Kedziora-Chudczer, L., Tzioumis, A. K., & Macquart, J.-P. 2003, Ap&SS, 288, 63

Jauncey, D. L., & Macquart, J.-P. 2001, A&A, 370, L9

Jenkins, E. B., Savage, B. D., & Spitzer, L., Jr. 1986, ApJ, 301, 355

Jones, A. P., Tielens, A. G. G. M., & Hollenbach, D. J. 1996, ApJ, 469, 740

Jones, A. P., Tielens, A. G. G. M., Hollenbach, D. J., & McKee, C. F. 1994, ApJ, 433, 797

Kalas, P., Liu, M. C., & Matthews, B. C. 2004, Science, 303, 1990

Kedziora-Chudczer, L. 2006, MNRAS, 369, 449

Lagrange-Henri, A. M., Ferlet, R., Vidal-Madjar, A., Beust, H., Gry, C., & Lallement, R. 1990, A&AS, 85, 1089

Lallement, R., & Bertin, P. 1992, A&A, 266, 479

Lallement, R., Bertin, P., Ferlet, R., Vidal-Madjar, A., & Bertaux, J. L. 1994, A&A, 286, 898

Lallement, R., Ferlet, R., Lagrange, A. M., Lemoine, M., & Vidal-Madjar, A. 1995, A&A, 304, 461

Lallement, R., Raymond, J. C., Bertaux, J.-L., Quémerais, E., Ko, Y.-K., Uzzo, M., McMullin, D., & Rucinski, D. 2004, A&A, 426, 867

Lallement, R., Welsh, B. Y., Vergely, J. L., Crifo, F., & Sfeir, D. 2003, A&A, 411, 447

Lehner, N., Jenkins, E. B., Gry, C., Moos, H. W., Chayer, P., & Lacour, S. 2003, ApJ, 595, 858

Lemoine, M., Vidal-Madjar, A., Bertin, P., Ferlet, R., Gry, C., & Lallement, R. 1996, A&A, 308, 601

Linsky, J. L., Redfield, S., Wood, B. E., & Piskunov, N. 2000, ApJ, 528, 756

Linsky, J. L., Rickett, B. J., & Redfield, S. 2008, ApJ, in press (arXiv: 0711.1144)

Linsky, J. L., & Wood, B. E. 1996, ApJ, 463, 254

Linsky, J. L., et al. 2006, ApJ, 647, 1106

Lovell, J. E. J., et al. 2007, in ASP Conf. Ser. 365, SINS—Small Ionized and Neutral Structures in the Diffuse Interstellar Medium, ed. M. Haverkorn & W. M. Goss (San Francisco: ASP), 279

Macquart, J.-P., & de Bruyn, A. G. 2006, A&A, 446, 185

McClintock, W., Henry, R. C., Linsky, J. L., & Moos, H. W. 1978, ApJ, 225, 465

McCray, R., & Snow, T. P., Jr. 1979, ARA&A, 17, 213

McKee, C. F., & Ostriker, J. P. 1977, ApJ, 218, 148

Meyer, D. M., Lauroesch, J. T., Heiles, C., Peek, J. E. G., & Engelhorn, K. 2006, ApJ, 650, L67

Möbius, E., et al. 2004, A&A, 426, 897

Müller, H.-R., Frisch, P. C., Florinski, V., & Zank, G. P. 2006, ApJ, 647, 1491

Putney, M. L., & Stinebring, D. R. 2006, Chinese J. Astron. Astrophys. Suppl., 6, 233

Redfield, S. 2006, in ASP Conf. Ser. 352, New Horizons in Astronomy, ed. S. J. Kannappan et al. (San Francisco: ASP), 79

Redfield, S., Kessler-Silacci, J. E., & Cieza, L. A. 2007, ApJ, 661, 944

Redfield, S., & Linsky, J. L. 2000, ApJ, 534, 825

———. 2001, ApJ, 551, 413

———. 2002, ApJS, 139, 439

———. 2004a, ApJ, 602, 776

———. 2004b, ApJ, 613, 1004

Rickett, B. J., Kedziora-Chudczer, L., & Jauncey, D. L. 2002, ApJ, 581, 103

Rickett, B. J., Witzel, A., Kraus, A., Krichbaum, T. P., & Qian, S. J. 2001, ApJ, 550, L11

Roberge, A., Weinberger, A. J., Redfield, S., & Feldman, P. D. 2005, ApJ, 626, L105

Savage, B. D., & Sembach, K. R. 1996, ARA&A, 34, 279

Slavin, J. D., & Frisch, P. C. 2002, ApJ, 565, 364

Smirnova, T. V., Gwinn, C. R., & Shishov, V. I. 2006, A&A, 453, 601

Stokes, G. M. 1978, ApJS, 36, 115

Vallerga, J., Lallement, R., Lemoine, M., Dalaudier, F., & McMullin, D. 2004, A&A, 426, 855

Vallerga, J. V., Vedder, P. W., Craig, N., & Welsh, B. Y. 1993, ApJ, 411, 729

Vázquez-Semadeni, E., Ryu, D., Passot, T., González, R. F., & Gazol, A. 2006, ApJ, 643, 245

Vennes, S., & Lanz, T. 2001, ApJ, 553, 399

Wakker, B. P., & Mathis, J. S. 2000, ApJ, 544, L107

Welsh, B. Y., Craig, N., Vedder, P. W., & Vallerga, J. V. 1994, ApJ, 437, 638

Welty, D. E., Hobbs, L. M., & Kulkarni, V. P. 1994, ApJ, 436, 152

Witte, M. 2004, A&A, 426, 835

Witte, M., Rosenbauer, H., Banaszkiewicz, M., & Fahr, H. 1993, Adv. Space Res., 13, 121

Wolfire, M. G., Hollenbach, D., McKee, C. F., Tielens, A. G. G. M., & Bakes, E. L. O. 1995a, ApJ, 443, 152

Wolfire, M. G., McKee, C. F., Hollenbach, D., & Tielens, A. G. G. M. 1995b, ApJ, 453, 673

Wood, B. E. 2004, Living Rev. Sol. Phys., 1, 2

Wood, B. E., Alexander, W. R., & Linsky, J. L. 1996, ApJ, 470, 1157

Wood, B. E., Ambruster, C. W., Brown, A., & Linsky, J. L. 2000, ApJ, 542, 411

Wood, B. E., Müller, H.-R., Zank, G., Linsky, J., & Redfield, S. 2005a, ApJ, 628, L143

Wood, B. E., Redfield, S., Linsky, J. L., Müller, H.-R., & Zank, G. P. 2005b, ApJS, 159, 118

Yan, H., Lazarian, A., & Draine, B. T. 2004, ApJ, 616, 895

Zank, G. P. 1999, Space Sci. Rev., 89, 413